Extensive Holocene West Antarctic Ice Sheet retreat and rebound-driven re-advance

Authors:

J. Kingslake[1]*, R. Scherer[2]*, T. Albrecht[3]*, J. Coenen[2], R. Powell[2], R. Reese[3], N. Stansell[2], S. Tulaczyk[4], M. Wearing[1], P. L. Whitehouse[5]

Affiliations:

1 Lamont-Doherty Earth Observatory, Columbia University, New York, USA

2 Department of Geology and Environmental Geosciences, Northern Illinois University, Illinois, USA

3 Potsdam Institute for Climate Impact Research (PIK), Member of the Leibniz Association, Potsdam, Germany

4 Earth & Planetary Sciences Department, University of California Santa Cruz, Santa Cruz, CA, USA

5 Department of Geography, Durham University, Durham, UK

* These authors contributed equally to this work.

Correspondence to: J. Kingslake (j.kingslake@columbia.edu)

Keywords: West Antarctic Ice Sheet, Grounding Line, Ross Ice Shelf, Ronne Ice Shelf, ice-penetrating radar, radiocarbon, PISM Parallel Ice Sheet Model, ice rise, isostatic rebound

Numerical models used to predict future ice-sheet contributions to sea-level rise use reconstructions of post-Last Glacial Maximum (LGM) ice-sheet retreat to tune model parameterizations[1]. West Antarctic Ice Sheet (WAIS) reconstructions have assumed progressive retreat throughout the Holocene[2,3,4], due to a lack of broad-scale evidence for a more complex history. Here we show that the WAIS grounding line (GL) retreated several hundred kilometers inland of today's GL, before Holocene isostatic rebound caused it to re-advance to its current position. Evidence includes (1) radiocarbon in sediment cores recovered from beneath Ross Sea Sector ice streams, indicating widespread Holocene marine exposure and (2) ice-penetrating radar observations of englacial structure in the Weddell Sea Sector, indicating ice-shelf grounding. We explore the implications of these findings with an ice-sheet model. Modelled GL re-advance requires ice-shelf grounding caused by isostatic rebound. Our findings overturn the assumption of progressive Holocene GL retreat in West Antarctica and corroborate previous suggestions of ice sheet re-advance[5]. Rebound-driven stabilizing processes were apparently able to halt and reverse climate-initiated ice loss. Whether these processes can reverse present-day loss[6] on millennial timescales depends on bedrock topography and mantle viscosity – parameters that are difficult to measure and to incorporate into ice-sheet models.

Recent evidence suggests that Holocene GL migration in some areas of West Antarctica was more complex than previously assumed[5,7,8]. In the Weddell and Ross Sea sectors, anomalies in radar-observed englacial structure[9,10] and isostatic rebound rates[5] suggest that the GL was recently upstream of its current location. Rebound has been suggested as a negative feedback on ice-sheet retreat[11,12,13,14] and as a possible cause of GL re-advance[5], via the grounding of ice shelves[15,16]. Better constraints on GL history are important. If this history differs significantly from often-used ice-sheet reconstructions[2] over wide areas, better constrains on past changes could lead to improved ice-sheet models[1] and measurements of ice-sheet mass change[17]. To this end, we present new evidence for widespread Holocene GL re-advance in Antarctica from subglacial sediments and radar-observed englacial structure.

Multiple boreholes drilled through the Ross Ice Shelf (RISP, WGZ) and the Whillans (WIS/UpB, SLW), Kamb (KIS) and Bindschadler (BIS) ice streams[18] allowed recovery of subglacial sediment cores up to 200 km inland of the present Ross Sea Sector GL (Fig. 1). Radiocarbon analyses of 36 till samples indicate the widespread presence of young organic carbon stratigraphically distributed through the upper meter(s) of till. Total organic carbon concentration is low, ranging from 0.2 to 0.4%, the majority of which is derived from Tertiary marine deposits[19]. Nevertheless, organic carbon in all subglacial sediments analyzed includes readily measurable radiocarbon (Extended Data Table 1).

Basal melting of meteoric ice is a negligible source of radiocarbon to the subglacial environment (Methods). Subglacial microbes cannot introduce young carbon, as they rely on legacy carbon[21]. Contamination of samples by modern carbon is discounted because samples were curated and sealed in different laboratories, yet yielded consistent results. Hydropotential gradients[20] and high basal water pressures[18] drive subglacial water towards the GL in this region, discounting subglacial transport of ^{14}C-bearing materials from the ocean to the core sites. In contrast, observations of an active marine community just downstream of the GL, more than 600 km from the open ocean (Methods), demonstrate that radiocarbon is introduced virtually everywhere that ocean waters reach beneath the ice shelf.

We conclude that a small proportion of the organic carbon contained in the sediments was laid down under sub-ice shelf conditions at or upstream of the sediment cores recently enough to allow persistence of measurable radiocarbon. This implies that the Siple-Gould Coast GL was at least 200 km inland of its current position sometime after the LGM. Calculated radiocarbon ages (Extended Data Table 1) are probably significantly older than the most recent marine incursion, due to dilution by more abundant radiocarbon dead material[4, 21] (Methods; Extended Data Fig. 5). Ice flow transports till downstream[18], so the GL may have retreated even farther inland than the core sites (Fig. 1). The proximity of the cores to Siple Dome (SD; Fig. 1), where 350 m of thinning coincided with rapid sea-level rise during Meltwater Pulse 1a (MWP-1a) around 14.5 kyr before present (BP) (ref. 22), hints that MWP-1a could have triggered GL retreat, though this does not necessarily imply a significant WAIS sea-level contribution to MWP-1a (ref. 4).

On the other side of the WAIS we conducted a 700 km-long ground-based ice-penetrating radar survey of Henry Ice Rise (HIR; Figs. 1 & 2; Methods). HIR is 7000 km^2 in area and grounded 310-800 m below sea level. Our survey revealed englacial structures inconsistent with present-day slow (<10 m a^{-1}) and cold-based flow conditions (Methods).

A series of steep englacial reflectors (Fig. 2d) cluster around a basal topographic high at the northern end of HIR (Fig. 2a). These features intercept the bed, penetrate to 200-300 m above the bed and cross-cut smoothly-undulating isochrones (Fig. 2d; Extended Data Fig. 2). They have similar lateral extents, orientations and spacing to extensional surface crevasses at Doake Ice Rumples (DIR; Fig. 1; Extended Data Fig. 1). At ice rumples, ice that was floating upstream flows onto and over a bedrock high. We interpret the buried features in HIR as marine-ice-filled relic crevasses formed when ice-rumple flow persisted on HIR. The crevasses were probably near-vertical while active and have been buried and deformed to varying extents into steeply-dipping structures by complex ice flow (Methods). Further evidence that parts of HIR were previously floating include prominent synclines in internal isochronal layers that increase in amplitude with depth, are unrelated to basal topography and truncate at the bed (Figs. 2b, 2c, Extended Data Fig. 2) – characteristics indicative of past ocean melting[9].

Ice-shelf grounding on the topographic high beneath HIR – first forming ice rumples, then thickening to form the ice rise – can explain the unusual englacial structures. Contact with the ocean generates isochrone synclines where melting is focused at a static GL for long enough[23]. Ice-rumple flow generates surface crevasses similar to those observed on and downstream of DIR, which were preserved in HIR as flow stagnated. Prior to grounding, the ice shelf likely flowed approximately northward in the location of HIR. Post-grounding thickening upstream of the topographic high explains today's configuration, with the initial grounding point beneath HIR's northern extreme. An alternative interpretation is that HIR persisted throughout the Holocene and recently grew to its current size. However, we argue that complete ungrounding is more likely (Methods). Under either scenario, we interpret a contrast in surface texture, approximately coincident with the onset of relic crevassing (Fig. 2b), as a signature of a past GL configuration (Methods). The formation or re-growth of HIR is expected to have increased the buttressing force exerted by the Ronne Ice Shelf on the upstream ice sheet, with implications for GL migration and mass balance.

To explore the cause and implications of ice-rise formation (revealed by radar observations) and ice stream GL retreat and re-advance (revealed by radiocarbon analyses), we turn to numerical ice-sheet modelling. We simulate the post-LGM evolution of the WAIS using the Parallel Ice Sheet Model (PISM)[24] with improved descriptions of sub-shelf melting and solid Earth rebound, forced by paleo-sea-level and ice-core temperature reconstructions (Methods). A model ensemble investigated first-order sensitivities to independent variations in parameters related to ice flow, glacial isostatic adjustment (GIA), calving, sub-shelf melting, basal traction and accumulation (Methods).

After partially compensating for uncertainty in bed topography (Methods), our simulations display remarkable agreement with the conclusions of our radiocarbon and radar analyses. Our reference simulation (Methods) demonstrates this agreement (Fig. 3; Supplementary Video 1). In this simulation, rising sea level and surface temperatures during the last glacial termination drive GL retreat through regions currently occupied by the Ronne and Ross ice shelves. The GL reaches a quasi-stable position around 10 kyr BP, up to approximately 300 km inland of the present-day GL (Fig. 3; Extended Data Fig. 3). Retreat exposes nearly all of our core sites and the bed of HIR to the ocean. Approximately 352,000 km^2 of the area currently covered by grounded ice ungrounds during retreat, resulting in lithospheric rebound of up to 175 mm yr^{-1}. The rising bed eventually causes the Ross and Ronne ice shelves to ground on bathymetric highs in the locations of present-day ice rises, including HIR. Ice-rise formation increases ice-shelf buttressing, causing the GL to re-advance towards its present-day location (Fig. 3; Extended Data Fig. 4; Methods). In the Amundsen Sea Sector, the GL retreats to its modern position without significant inland retreat and re-advance.

Rebound-driven re-advance causes WAIS to gain ice above flotation equivalent to 33 cm of sea level fall during this simulation (Weddell Sector, 2 cm; Ross Sector, 31 cm). Ice-volume minima in each sector are asynchronous and the minimum in whole ice-sheet volume occurs 1.5 kyr BP, at which time the ice sheet is 20 cm sea-level equivalent smaller than present.

The timing and magnitude of simulated GL retreat and re-advance depend on model parameters, forcings, bed topography and spatial resolution (Extended Data Figs. 6 & 7; Methods). For example, increasing mantle viscosity expedites retreat, increases maximum retreat and delays re-advance. Ice-rise formation greatly enhances GL re-advance and is sensitive to bed topography, which is regionally uncertain, and dynamically-relevant topographic features are poorly-represented at the spatial resolution of the model (Extended Data Fig. 4; Methods).

Notably, although GL re-advance was not their focus, four previous Antarctic ice-sheet modelling studies, employing alternative parameterizations of basal sliding, GL flux and lithosphere response, also simulate Holocene GL retreat and re-advance in these sectors in some simulations[25,26,27,28].

Radiocarbon in subglacial sediments, radar-observed relic crevassing and ice-sheet modelling, provide corroborating evidence that two large Antarctic catchments re-advanced to their present-day configurations during the Holocene (Fig. 3). Previous work is consistent with this conclusion, but cannot confirm or rule-out Holocene retreat and re-advance (Methods). Moreover, previous authors have found evidence for localized re-advance and suggested rebound as a cause[5,10]. However, ice-sheet reconstructions used to tune ice-sheet models and correct mass balance observations currently do not include large-scale GL re-advance[1,2]. Updating these reconstructions to include re-advance could impact ice-sheet gravimetry and altimetry[17], and sea-level projections. Furthermore, we hypothesize that the GL in the Weddell and Ross Sea Sectors may be capable of retreating far inland of its current position without triggering runaway ice-sheet collapse.

Our model does not simulate retreat and rebound-driven re-advance in the Amundsen Sea Sector (Fig. 3), where present-day GL retreat is causing concern about future runaway collapse[6] and recent re-advance could explain observed sub-shelf iceberg ploughmarks[29]. Our findings motivate future work to examine if rebound-driven mechanisms could slow or reverse this retreat on millennial timescales.

Rising eustatic sea-level and temperatures were major climate-related drivers of ice-sheet retreat during and after the last glacial termination. In contrast, it appears that climate-independent lithospheric rebound and ice-shelf grounding were the main drivers of Holocene GL re-advance. The impact of rebound on the ice sheet depends sensitively on bedrock topography and mantle viscosity (Methods). Accurate mapping of potential grounding points and improved parameterization of uplift are needed to forecast the direction and rate of future GL migration in West Antarctica.

References

[1] DeConto, R. M. & Pollard, D. Contribution of Antarctica to past and future sea-level rise. *Nature* **531,** 591–597 (2016).

[2] Bentley, M. J. Cofaigh, C. Ó. Anderson, J. B. et al. A community-based geological reconstruction of Antarctic Ice Sheet deglaciation since the Last Glacial Maximum. *Quat. Sci. Rev.* **100,** 1–9 (2014).

[3] Conway, H. Hall, B. L. Denton, G. H. et al. Past and future grounding-line retreat of the West Antarctic Ice Sheet. *Science* **286,** 280–283 (1999).

[4] Spector, P. Stone, J. Cowdery, S. G. et al. Rapid Early-Holocene Deglaciation in the Ross Sea, Antarctica. *Geophys. Res. Lett., 44, 7817–7825,* doi:10.1002/2017GL074216 (2017).

[5] Bradley, S. L. Hindmarsh, R. C. A. Whitehouse, P. L. et al. Low post-glacial rebound rates in the Weddell Sea due to Late Holocene ice-sheet readvance. *Earth Planet. Sci. Lett.* **413,** 79–89 (2015).

[6] Scambos, T.A., Bell, R.E., Alley, R.B., Anandakrishnan, S., Bromwich, D.H., Brunt, K., Creyts, T.T., Das, S.B., DeConto, R., Dutrieux, P. and Fricker, H.A. How much, how fast?: A science review and outlook for research on the instability of Antarctica's Thwaites Glacier in the 21st century. *Global and Planetary Change* **153**, 16-34 (2017).

[7] Goodwin, I. D. Did changes in Antarctic ice volume influence late Holocene sea-level lowering? *Quat. Sci. Rev.* **17,** 319–332 (1998).

[8] Halberstadt, A.R.W., Simkins, L.M., Greenwood, S.L. and Anderson, J.B., Past ice-sheet behaviour: Retreat scenarios and changing controls in the Ross Sea, Antarctica. *Cryosphere*, **10**(3), (2006)

[9] Catania, G. A. Conway, H. Raymond, C. F. et al. Evidence for floatation or near floatation in the mouth of Kamb Ice Stream, West Antarctica, prior to stagnation. *J. Geophys. Res. Earth Surf.* **111,** (2006).

[10] Siegert, M. Ross, N. Corr, H. et al. Late Holocene ice-flow reconfiguration in the Weddell Sea sector of West Antarctica. *Quat. Sci. Rev.* **78,** 98–107 (2013).

[11] Adhikari, S., Ivins, E.R., Larour, E., Seroussi, H., Morlighem, M. and Nowicki, S. Future Antarctic bed topography and its implications for ice sheet dynamics. Solid Earth, 5(1), 569 (2014)

[12] Gomez, N. Pollard, D. & Holland, D. Sea-level feedback lowers projections of future Antarctic Ice-Sheet mass loss. *Nat. Commun.* **6,** 8798 (2015).

[13] Greischar, L. L. & Bentley, C. R. Isostatic equilibrium grounding line between the West Antarctic inland ice sheet and the Ross Ice Shelf. *Nature* **283,** 651–654 (1980).

[14] Konrad, H. Sasgen, I. Pollard, D. et al. Potential of the solid-Earth response for limiting long-term West Antarctic Ice Sheet retreat in a warming climate. *Earth Planet. Sci. Lett.* **432,** 254–264 (2015).

[15] Matsuoka, K. Hindmarsh, R. C. A. Moholdt, G. et al. Antarctic ice rises and rumples: Their properties and significance for ice-sheet dynamics and evolution. *Earth Sci. Rev.* **150,** 724–745 (2015).

[16] Thomas, R. H. The creep of ice shelves: interpretation of observed behavior. *J. Glaciol.* **12,** 55–70 (1973).

[17] Hanna, E., Navarro, F.J., Pattyn, F., Domingues, C.M., Fettweis, X., Ivins, E.R., Nicholls, R.J., Ritz, C., Smith, B., Tulaczyk, S. and Whitehouse, P.L. Ice-sheet mass balance and climate change. Nature, **498**(7452), 51 (2013)

[18] Kamb, B. Basal zone of the West Antarctic ice streams and its role in lubrication of their rapid motion. *The West Antarctic ice sheet: behavior and environment* (eds R. B. Alley and R. A. Bindschadler) American Geophysical Union, Washington, D. C.. 157–199 (2001). doi: 10.1029/AR077p0157

[19] Scherer, R. P. Quaternary and tertiary microfossils from beneath ice stream B: evidence for a dynamic West Antarctic ice sheet history. *Palaeogeogr. Palaeoclimatol. Palaeoecol.* **90,** 395–412 (1991).

[20] Livingstone, S. Clark, C. Woodward, J. et al. Potential subglacial lake locations and meltwater drainage pathways beneath the Antarctic and Greenland ice sheets. *Cryosphere* **7,** 1721–1740 (2013).

[21] Christner, B. C. Priscu, J. C. Achberger, A. M. et al. A microbial ecosystem beneath the West Antarctic ice sheet *Nature* **512,** 310–313 (2014).

[22] Price, S. F. Conway, H. & Waddington, E. D. Evidence for late Pleistocene thinning of Siple Dome, West Antarctica. *J. Geophys. Res. Earth Surf.* **112,** (2007).

[23] Catania, G. Hulbe, C. & Conway, H. Grounding-line basal melt rates determined using radar-derived internal stratigraphy. *J. Glaciol.* **56,** 545–554 (2010).

[24] Winkelmann, R. Martin, M. A. Haseloff, M. et al. The Potsdam parallel ice sheet model (PISM-PIK)-Part 1: Model description. *The Cryosphere* **5,** 715 (2011).

[25] Pollard, D. Chang, W. Haran, M. et al. Large ensemble modeling of the last deglacial retreat of the West Antarctic Ice Sheet: comparison of simple and advanced statistical techniques. *Geosci. Model Dev.* **9,** 1697–1723 (2016).

[26] Golledge, N. R. Menviel, L. Carter, L. et al. Antarctic contribution to meltwater pulse 1A from reduced Southern Ocean overturning. *Nat. Commun.* **5,** 5107 (2014).

[27] Maris, M. N. A. Van Wessem, J. M. Van De Berg, W. J. et al. A model study of the effect of climate and sea-level change on the evolution of the Antarctic Ice Sheet from the Last Glacial Maximum to 2100. *Climate Dyn.* **45,** 837–851 (2015).

[28] Pollard, D., Gomez, N., & Deconto, R. M. Variations of the Antarctic ice sheet in a coupled ice sheet-Earth-sea level model: Sensitivity to viscoelastic Earth properties. *J. Geophys. Res. Earth Surf.* **122**, https://doi.org/10.1002/2017JF004371 (2017).

[29] Graham, A.G., Dutrieux, P., Vaughan, D.G., Nitsche, F.O., Gyllencreutz, R., Greenwood, S.L., Larter, R.D. and Jenkins, A. Seabed corrugations beneath an Antarctic ice shelf revealed by autonomous underwater vehicle survey: origin and implications for the history of Pine Island Glacier. Journal of Geophysical Research: Earth Surface, 118(3), 1356-1366 (2013)

Supplementary Information

A supplementary video accompanies this submission.

Acknowledgements

JK and the Weddell Sea fieldwork were funded by Natural Environmental Research Council grant NE/J008087/1, led by Richard Hindmarsh. Logistical support was provided by many members of the British Antarctic Survey's air unit and field operations team. Thank you particularly to Iain Rudkin and Scott Webster for assistance in the field. Thank you also to Schlumberger Limited for a software donation.

PISM development is supported by NASA grants NNX13AM16G and NNX13AK27G. TA is supported by the Deutsche Forschungsgemeinschaft (DFG) in the framework of the priority program "Antarctic Research with comparative investigations in Arctic ice areas" by grant LE1448/6-1 and LE1448/7-1.We gratefully acknowledge the European Regional Development Fund, the German Federal Ministry of Education and Research and the Land Brandenburg for providing high performance computer resources at the Potsdam Institute for Climate Impact Research. We also thank the Gauss Centre for Supercomputing e.V. (www.gauss-centre.eu) for providing computing time on the GCS Supercomputer SuperMUC at Leibniz Supercomputing Centre (www.lrz.de) (project: pr94ga). We thank Christo Buizert for providing ice-core temperature reconstructions, Dick Peltier for access to eustatic sea-level reconstructions, Jan Lenaerts for RACMO surface mass balance data and Stewart Jamieson for providing the RAISED consortiums grounding line reconstructions.

RS, JC, RP and ST were funded by NSF WISSARD Project grants ANT-0839107, ANT-0839142, ANT-0838947 and ANT-0839059. Subglacial sediment sample collection at Subglacial Lake Whillans and Whillans Grounding Zone was facilitated by the United States

Antarctic Program and efforts of multiple field support teams, including the drilling team from the University of Nebraska–Lincoln, the WISSARD traverse personnel, as well as by Air National Guard and Kenn Borek Air who provided air support. WIS, KIS and BIS samples were recovered by Barclay Kamb's program at California Institute of Technology (1988-2001), including RS and ST, and samples from the US Antarctic Program’s Ross Ice Shelf Project (1977-1979) cores were made available for study by the US Antarctic Sediment Core Repository, Florida State University. PLW is funded by a NERC Independent Research Fellowship (NE/K009958/1). This research is a contribution to the SCAR SERCE program.

We thank Robert Arthern, Robin Bell, Richard Hindmarsh, Carlos Martín, John Southon, Kirsty Tinto for discussions that contributed to this study. We particularly thank David Pollard for sharing ideas and unpublished Penn State model outputs for discussion.

Author contributions statement

All authors contributed to manuscript preparation. TA, JK and RS are co-lead authors with equal contributions; others are listed alphabetically. JK designed and conducted the Weddell Sea Sector ice-penetrating radar survey and led the preparation of the manuscript. RS, JC, RP, and ST collected and analyzed sub-ice sediment samples as part of the WISSARD and earlier drilling projects in the Ross Sea Sector. NS and JC prepared samples and interpreted ^{14}C and ^{13}C results. TA ran the PISM simulations with extended analysis of parameter sensitivity. RR designed and analyzed experiments for disentangling drivers of re-advance. MW analyzed radar data from the Weddell Sea Sector. PLW provided input on parameterization of solid Earth rebound and sea-level forcing for the model experiments.

Additional information

Reprints and permissions information is available at www.nature.com/reprints. The authors declare no competing financial interests. Correspondence and requests for materials should be addressed to j.kingslake@columbia.edu.

Figure 1: Basal topography and surface ice flow speed in the Weddell and Ross sea sectors of West Antarctica. a, Basal topography and bathymetry[30] and **b,** ice-surface flow speed[31] in the Ross Sea Sector. The locations of sediment recovery are shown in green. **c**, Basal topography and bathymetry [30] and **d**, flow speed[31] in the Weddell Sea Sector. In all panels the present-day GL[32] is in red, the (asynchronous) modelled minimum extent of the GL in each sector is in blue. Axes show polar stereographic coordinates in km. Insets show locations in West Antarctica. Labels not defined in the text: Whillans Ice Stream (WIS), Subglacial Lake Whillans (SLW), Ross Ice Shelf Project (RISP)[33]. Also labelled are the Institute, Möller and Foundation Ice Streams.

Figure 2: Ice-penetrating radar evidence for grounding of the Ronne Ice Shelf. a, Radar-derived ice-bed elevation beneath HIR. See Fig. 1c for location in the Weddell Sea Sector. The present-day GL[32] is in red. **b**, Radar lines coloured according to where relic crevasses are found. **c,** Normalized elevation ζ_i of an isochrone (Methods). Background images in **a**–**c** are from the MODIS mosaic of optical (red band) imagery over Antarctica (MOA), which reveals Antarctic surface morphology[34,35]. Green curves in **b** and **c** highlight a contrast in surface texture (Methods), running parallel to the present-day GL, the onset of relic crevassing and, on the East side, a prominent isochrones syncline **d**, Radargram displaying examples of undulating isochrones. One isochrone is mapped using the colour map from **c**. **e**, Close-up view of near-bed relic crevasses with mean spacing of approximately 450 m.

Figure 3: Modelled grounding-line retreat and re-advance due to lithospheric rebound. WAIS GL position in the reference simulation at 20 kyr BP (violet), with a recent LGM ice-sheet reconstruction in black (ref. 2, scenario B). The ice sheet asynchronously reaches a minimal extent in the Weddell and Ross sea sectors at 10.2 kyr BP and 9.7 kyr BP respectively (blue). The GL re-advances towards its present-day GL location[30] (red). Final simulated GL position is in green. The locations of Siple-Gould Coast sediment cores and selected ice rises are indicated. Brown dashed lines show cross-sections used for Extended Data Figs 3, 6 & 7. Red dotted lines show longitude-defined sectors. Background shading shows basal topography and bathymetry[30].

Methods

Sediments

Radiocarbon and ^{13}C analyses of glacial tills.

Subglacial sediments have been recovered during multiple field seasons by hot-water drilling through the southern Ross Ice Shelf and grounded West Antarctic Ice Sheet. Sub-ice shelf core samples include the Ross Ice Shelf Project (RISP, 1978) and the Whillans Ice Stream Grounding Zone (WGZ, 2015), recovered as part of the Whillans Ice Stream Subglacial Access Research Drilling (WISSARD) Project. The WISSARD Project also included cores from beneath grounded ice at Subglacial Lake Whillans (SLW, 2013). Sub-ice stream samples further upstream were recovered from the Whillans (WIS/UpB, 1989, 1991, 1995, SLW, 2013), Kamb (KIS, 1995, 1996, 2000) and Bindschadler (BIS, 1998) ice streams[18]. The sediments recovered are tills with a matrix derived in part from strata that accumulated during multiple intervals of terrestrial, coastal and open marine deposition in West Antarctica. Source strata integrated into the tills are dated by microfossils[36,37]. They include terrestrial plant spores dating back to the Devonian, but are dominantly Miocene age diatoms, reflecting the abundance of Miocene marine strata in the embayment. The youngest diatoms present are of Pleistocene age, representing direct precipitation in open water during intervals of past ice sheet collapse during MIS-5e (120 kyr BP) or earlier Pleistocene interglacials[38]. These microfossils predate any measurable radiocarbon source in the sub-glacial environment.

Bulk sediment samples for radiocarbon measurements were wet sieved with nanopure water through a 63-µm screen to remove coarser mineral matter, then pre-treated using standard acid-base-acid protocols[39]. The remaining insoluble fraction for each sample was combusted to convert to CO_2 and then graphitized. Samples were then measured using accelerator mass spectrometry at the W.M. Keck Carbon Cycle Laboratory at the University of California, Irvine.

A subset of samples was also independently pretreated and measured at the Uppsala radiocarbon facility, Sweden, following the same protocol. Due to the inherent age uncertainties, radiocarbon “ages” are presented as raw, uncalibrated values that are not corrected for known reservoir effects. Acid-insoluble organic ^{13}C ratios were generated separately at the Environmental Isotope Lab at University of Arizona, following standard methods.

In order to minimize the potential for contamination of small samples during analysis, we processed large samples (>150 mg), producing ~1 to 2 mg of carbon that was combusted and reduced to graphite, while simultaneously processing numerous primary and secondary standards, ranging in size from very small (<0.1 mg) to large (1.8 mg). To further demonstrate that we have thoroughly explored a wide range of radiocarbon systematics, we also dated base-soluble fractions for a subset of samples. The base-soluble fraction (humic acid) resulted in ages that were somewhat older (~1 to 2 ka) than the bulk sediment samples. These age differences are not significant and the results are consistent with our other findings. Multiple fractions that yield similar ages further rule out contamination as a possible explanation of our radiocarbon results.

We considered and ruled out sample contamination by modern carbon prior to analysis as a potential explanation of the radiocarbon results. Subglacial samples were recovered between 1989 and 2013 and sub-ice shelf samples were recovered in 2015 (WGZ) and 1978 (RISP). SLW (2013) samples were recovered and handled using full clean-access protocols[40], where all instruments were peroxide washed prior to recovery. Cores and samples were sealed and maintained in a +4 ^{o}C environment. Clean access protocols were not employed during earlier sample recovery (WIS, KIS and BIS), though every effort was made to maintain appropriate cleanliness in the field and in the laboratory. These samples were sealed and maintained at 4 C. Subsamples were stored in sealed sections of plastic core liner, plastic bags or in plastic vials. Many of the samples in vials dried out and some of the dried samples have been stored at room temperature in the intervening years. The fact that the older subglacial samples demonstrate the oldest apparent radiocarbon ages argues against introduction of new carbon from microbial or fungal growth on the sample. RISP cores were stored at the Florida State University Antarctic sediment core repository, sealed and chilled. The somewhat younger ages there are readily explained by the long-term exposure to the sub-ice shelf ocean cavity. Despite the different sample storage methods used, radiocarbon results are very consistent, which argues against contamination. Given the small concentration of organic carbon in the samples, a very small amount of contamination with modern carbon would result in some anomalous younger ages, yet all of our results fall within a narrow range. Given the range of sample sources and storage methods, equal contamination of all the samples consistent with our results is extremely unlikely.

Apparent and true ages of sediments.

Given the dominant concentration of old (radiocarbon dead) organic carbon in the samples[41], all ages presented are older than the likely age of the pure radiocarbon component; note the calculated "percent modern" column in Extended Data Table 1. We infer post-LGM ages for all samples. Apparent radiocarbon ages for 11 till samples from beneath Whillans, Kamb, and Bindschadler ice streams were obtained for Acid Insoluble Organics (AIO) and span from ca. 20 to 35 kyr BP (Extended Data Fig. 5). Rare, small biogenic carbonate fragments from molluscs, foraminifera and calcareous nanofossils have been found in several samples, but these are all Tertiary in age, based on biostratigraphic assessment[19], and no attempt was made to radiocarbon date them.

Sediments recovered from beneath the southern Ross Ice Shelf (RISP cores; Fig. 1) were radiocarbon dated, generally yielding somewhat younger ages than the ice streams, likely reflecting the longer period of contact with the sub-ice shelf marine cavity. For the most part, the raw ages appear to correspond to the LGM of the WAIS, which started ca. 29 kyr BP and ended 13.9-15.2 kyr BP (ref. 42). Many lines of geologic evidence document that the LGM GL of the WAIS was located at or near the Ross Sea continental shelf break[43] at the time that corresponds with the apparent, uncorrected radiocarbon ages in our samples.

For the apparent ^{14}C ages to represent the true sediment ages, the GL of the WAIS would have to be upstream of the core sampling locations and also require all of the carbon pool in the samples to initially have had the standard, modern $^{14}C/^{12}C$ ratio. However, due to the large oceanic reservoir effect in Antarctica even modern amphipods sampled by us in January 2015 through a borehole at the GL of Whillans Ice Stream (WGZ; Fig. 1; Extended Data Table 1) had the fraction of modern radiocarbon at only 0.8669-08746, corresponding to apparent ages of 1075-1145 ^{14}C years. Moreover, it is well documented that radiocarbon dates on acid insoluble organic matter (AIO) obtained from bulk Antarctic glacigenic sediments are typically biased by admixture of old, ^{14}C-depleted organic matter[4,44,45,46]. This old organic material comes from glacial erosion of sediments deposited earlier in the Cenozoic[37]. The tills of the Ross ice streams are dominated by Tertiary, mostly Upper Miocene[37,38], marine source beds that are being actively eroded by grounded ice[36]. Given the uncertainty concerning the initial mixture between 'young' and 'old' sources of organic matter, we only know that the real age of the radiocarbon falls somewhere along the exponential-decay lines of ^{14}C in Extended Data Fig. 5, which intersect the left-hand vertical axes of this figure at the measured values of ^{14}C fraction modern.

Rather than the apparent ^{14}C ages representing the true sediment ages, it is more reasonable to assume that the WAIS GL was upstream of the till sampling locations subsequent to LGM, and that the calculated ages are biased toward older dates due to the high concentration of ancient carbon (Extended Data Fig. 5). Our assumption is also compatible with relatively low initial fractions of ^{14}C in sampled sediments, which we expect given that the sampled subglacial areas were exposed to influx of marine-sourced radiocarbon over a geologically short period of time and were located very far from the main locus of regional biological productivity in the Ross Sea. For instance, if our sediment samples received ^{14}C-bearing marine organics in the Mid Holocene, or ca. 5 kyr BP, the initial fractions of ^{14}C for these samples could be quite low (ca. 0.03 to 0.14) to explain the obtained apparent ages. In contrast, if one chooses a time period predating the WAIS LGM, say 30 kyr BP, most of our samples would need to have all of their organic matter completely equilibrated with the oceanic pool of ^{14}C at that time. Such conditions are difficult to find even in the modern open marine sediments of Ross Sea[44,45].

The balance of evidence favors post-LGM origin of ^{14}C-bearing organics in our till samples. However, the radiocarbon data do not allow us to pinpoint more precisely when the proposed retreat and re-advance of WAIS GL took place in the Ross Sea Sector of the ice sheet, or the specific duration of exposure.

Potential Input of Radiocarbon from Basal Melting.

Here we check if ^{14}C in subglacial sediment samples from beneath three different ice streams may have been entirely, or at least to significant extent, supplied by basal melting of meteoric ice. Meteoric ice may contain as much as 140 mm^3 of air per gram[47], which translates into ca. 0.02 grams of Total Inorganic Carbon (TIC) per m^3 of ice, assuming ice density of 910 kg/m^3 and pre-industrial Holocene atmospheric concentration of carbon dioxide (280 ppm). Meteoric ice also contains organic matter deposited from the atmosphere[48,49]. From the latter two publications we select 100 μg per liter as an upper bound on Total Organic Carbon (TOC) concentration in ice coming from the interior of the ice sheet. This assumption yields ca. 0.1 grams of TOC per m^3 of ice. TIC and TOC combined give 0.12 grams of carbon per m^3 of meteoric glacial ice. Basal melting rates vary beneath the Ross Sea Sector of the WAIS but 0.003

m/year provides a representative estimate for the region[50]. At this rate 0.36 grams of carbon per m^2 of the bed area would be entering the subglacial zone of the ice sheet in each thousand years. Some of this material would be entering subglacial sediments already as organic carbon melted out of the ice whereas the component derived from carbon dioxide trapped in the melting ice would exist as Dissolved Inorganic Carbon (DIC). We assume that the latter could be relatively quickly sequestered by subglacial microbial activity and converted into organic matter[21].

The basal flux of carbon estimated above needs to be compared to the total stock of carbon in the subglacial till from which our samples are derived. Our radiocarbon measurements show that ^{14}C is present at least within the top 1 m of till recovered from beneath three Ross Sea Sector ice streams. Analyses performed in the University of California, Santa Cruz stable isotope laboratory (UCSC CF-IRMS) on 27 subglacial sediment samples show average TOC of 0.33% (with standard deviation of 0.14%, both expressed in weight % of the dry sedimentary matter). Because the dry density of the till is ca. 1,600 kg m^{-3} (ref. 51), a 1m-thick layer of till contains about 5 kg of organic carbon per m^3 of sediment. Even if we assume that all of the carbon entering the subglacial zone with basal meltwater is sequestered within the top 1 m of till, it would take about 14 million years to supply the total amount of carbon found in these sediments just from basal melting at the rate of 0.36 grams per 1,000 years. Due to ^{14}C decay only the carbon released by basal melting during the last tens of thousands of years can contribute to the current stock of this radioisotope in till. The remaining ratio, R, of undecayed ^{14}C in a pool of carbon accumulating through time, t, by addition of new ^{14}C-bearing matter at a constant rate can be calculated from

$$R_{\{t\}} = \frac{R_0}{t}\int_0^t e^{-\frac{\varsigma}{\lambda}}\, d\varsigma = R_0 \frac{\lambda}{t}\left(1 - e^{-\frac{t}{\lambda}}\right),$$

where R_0 is the initial ^{14}C ratio (e.g., modern atmospheric ^{14}C /^{12}C ratio), ς is a dummy variable of integration, and λ is a constant given as the product of ^{14}C half life, 5,730 years, and the natural logarithm of 2 (i.e., 3,972 years). After 14 Myr the hypothetical subglacial carbon pool resulting solely from a continuous accumulation of carbon released from basal melting of meteoric ice would have average ^{14}C ratio of only 0.00028 of its initial (e.g., modern) value. This is two orders of magnitude too low to explain the fractions of ^{14}C measured in our samples. From the equation above we can calculate that the observed fractions of ^{14}C could only be explained by constant accumulation of carbon with modern initial ^{14}C over periods of time around 100 kyr years or less. However, the flux rate of carbon from basal melting would then have to be around 50 grams per thousand years per unit area of the ice base in order to explain the total stock of carbon in the sampled subglacial sediment layer (ca. 5 kg m^{-3}). As per our discussion above, such rates of carbon delivery from melting basal ice is implausibly high.

The analyses presented here did not even take into account the fact that any carbon released from the base of the ice streams has spent thousands to tens of thousands of years stored in the ice itself, which would further decrease its ^{14}C content. Furthermore, an ice stream base can also be composed of basal ice that has been formed by freezing of subglacial waters. Such basal ice would not contain ^{14}C-bearing carbon dioxide or organic matter. Hence, we conclude that release of ^{14}C from the base of the ice sheet does not represent a significant source and that inclusion of recent marine organic matter during a recent ice sheet retreat is needed to explain the concentrations of this isotope measured in our samples. Furthermore, the radiocarbon results we report are completely consistent with ice-sheet retreat ages inferred by the radar profiles and modeling reported here.

A modern analogy from the present-day sub-shelf cavity

Hot water drilling through 760 m of ice into 10 m of water in a sub-ice shelf embayment more than 600 km from the open ocean, at the Whillans Ice Stream grounding zone[52] (WGZ; Fig. 1) revealed a diverse community of organisms – including diverse amphipods, zoarcid and notothenioid fishes, and medusoid and ctenophorid jellies – thriving in fully-marine water. Radiocarbon analysis of appendages from 3 live-captured amphipods yielded raw ages between 1075±20 and 1145±20 yr BP (Extended Data Table 1), comparable to the Ross Sea surface water reservoir age[53]. This GL-proximal community of organisms demonstrates that radiocarbon is introduced from the open ocean virtually everywhere that ocean waters reach beneath the ice shelf. A retreating GL would have opened a subglacial marine environment that was immediately colonized by organisms that leave a radiocarbon tracer on their death. This modern sub-ice shelf process illustrates a likely pathway for Holocene radiocarbon to be deposited upstream of the current GL following past GL retreat. Furthermore, porewater chemistry indicative of seawater at Subglacial Lake Whillans (SLW; Fig. 1)[21] demonstrates that marine waters previously occupied the subglacial lake basin.

Henry Ice Rise: observations, interpretation and flow history.

Henry Ice Rise (HIR) is one of several ice rises in the Weddell Sea that influence the flow of Ronne Ice Shelf and its ice streams. It is currently slow-flowing[31] and cold based[54]. Based primarily on new ground-based ice-penetrating radar data, we hypothesise that HIR formed during the Holocene as the Ronne Ice Shelf grounded on a bathymetric high. Here we describe the radar system and our processing steps, and discuss possible links between surface roughness and englacial structure, which pertain to a potential past GL configuration. We also discuss an alternative interpretation that HIR existed throughout the Holocene, but was in the past significantly smaller than it is today.

Radar system

We used the British Antarctic Survey's DEep LOoking Radio-Echo Sounder (DELORES) on HIR to map basal topography and englacial structure[55]. A transmitter producing 2500 broadband radio-wave pulses per second was connecting to a 20 m, resistively-loaded dipole antenna, so that the center frequency of the system in ice was 4 MHz. A receiver unit, positioned 100 m from the transmitter connected to an identical dipole antenna was, triggered by the air wave and sampled the return signal at 250 MHz. The system was towed 50 m behind a snowmobile, driven at ~15 km hr^{-1}. After stacking, this configuration produced traces every ~85 cm along the track.

Data processing

Traces were geo-located in three dimensions using data from a dual-band GPS unit, mounted at the midpoint of the transmitter and receiver, then interpolated onto a regularly-spaced grid, band-pass filtered and compiled into radargrams. Radargrams were migrated with a 2D Kirchoff scheme, assuming a constant radio-wave velocity, 0.168 m ns^{-1} (ref. 55).

Elevations of the ice-bed interface and one of many englacial reflecting horizons, interpreted as isochrones, were determined using the software package Petrel by Schlumberger. The conversion from two-way travel time of the radar signal to depth was made assuming a constant radio-wave velocity (0.168 m ns^{-1}). Correcting for the impact of the lower density of the firn on radio-wave velocity would decrease the elevation by up to 10 m. As firn densities are unknown on HIR and likely vary spatially, we plot the uncorrected elevation of the ice-bed interface, z_b, (Fig. 2a). The normalized elevation of the isochrone ζ_i is computed from $\zeta_i = (z_i - z_b)/(z_s - z_b)$, where z_i is the elevation of the isochrone and z_s is the ice surface elevation measured with the dual-band GPS (Fig. 2c).

Surface texture contrasts visible in satellite imagery and surface elevation data.

Antarctic satellite imagery can be used to reveal subtle ice-surface topography[56]. The MODIS

Mosaic of Antarctica image in Fig. 2 highlights contrasting regions near the northern end of HIR, which we interpret as indicative of contrasting surface roughness. The green curves in Fig. 2b & 2c highlight the boundaries between the regions. The area between the two green curves appears smoother than the two regions between the green curves and the present-day GL. This interpretation is consistent with surface slopes estimated from elevation data collected by the GPS unit mounted on the DELORES radar system (not shown).

The surface-texture contrasts are approximately parallel to the present-day GL and align approximately with the following features reveled by our ice-penetrating radar survey: extensive synclines in internal isochrones (Fig. 2c; Extended Data Fig. 2a), locations where isochrones intercept the bed (Fig. 2b; Extended Data Fig. 2f) and the onset of buried crevasses (Fig. 2b). Here we explain these alignments by proposing that all these features are the signatures of a past GL configuration that persisted during a period either following the grounding of the ice rise, or alternatively, when HIR was at its minimum extent (see next section).

Today on the ice-shelf side of the eastern GL of HIR, ice undergoes lateral shear as the ice shelf moves past the relatively slow ice rise. This shear generates a region of dense crevassing (Extended Data Fig. 2g). Deformation in shear margins also warms englacial ice and generates ice-crystal fabric. Both can impact ice effective viscosity, as can crevassing. As the GL swept through the region between the surface-texture contrast and the present-day GL, crevasses generated on the ice-shelf side of the GL would have become inactive, buried and then deformed in the slow moving ice. Simultaneously, englacial temperature and crystal fabric would have evolved in a complex manner as the shear margin migrated in step with GL migration. We hypothesise that, along with spatially heterogeneous basal melting, these changes resulted in the complex pattern of tilted crevasses we observe today.

Under this interpretation, the rougher surface texture in the region currently occupied by buried crevasses (Fig. 2) results from spatially-variable ice viscosity caused by variability in the orientation and height of crevasses as well as spatially-variable ice fabric and temperature that have evolved enough to still affect ice flow. In contrast, the ice in the region between the two green curves (Fig. 2) has undergone a simpler flow history, without significant lateral shearing, either because it was immediately upstream of the initial location of grounding (the subglacial high in Fig. 2a) and experienced only longitudinal compression, or because it did not unground. We discuss the latter scenario next.

An alternative interpretation: a smaller-than-today, but persistent HIR

In the main text and in the previous section we interpret our radar observations to indicate that HIR became completely ungrounded post-LGM, then formed through re-grounding on the topographic high at the northern end of HIR. Some of our radar observations can be explained by an alternative ice-flow history. The GL surrounding HIR may have retreated significantly, exposing areas of the ice base to the ocean, where heterogeneous basal melting deformed and truncated isochrones at the bed. Subsequent re-advance of the GL would have buried crevassing as described above. This would have had an effect on regional ice-shelf dynamics and buttressing, but HIR would have persisted throughout the Holocene. However, if the locations where isochrones are truncated at the bed correspond to areas that ungrounded, then the simplest minimum extent suggested by mapping the layer truncations (Fig. 2b) would involve the ice rise ungrounding over the highest basal topography (Fig. 2a), while remaining grounded over deeper bathymetry. We do not yet understand ice-rise dynamics sufficiently to fully assess if this is possible. However, such a pattern of ungrounding during deglaciation is inconsistent with recent numerical modelling of idealized ice-rise formation[57]. Therefore, we argue that full ungrounding and later regrounding is more likely than partial ungrounding.

Whether the ice rise ungrounded completely or partially, the buttressing force exerted by the ice shelf on the ice sheet upstream would have been affected. These scenarios could be tested by drilling to the ice-rise base to obtain sediments for radiocarbon analysis and to allow measurement of the englacial temperature profile[58].

Ice-sheet modelling

Model description and forcings

We used the open-source Parallel Ice Sheet Model (PISM)[24,59,60], to perform pan-Antarctic simulations using glacial-cycle climate forcings. PISM is a three-dimensional, thermo-mechanically coupled ice-flow model with a freely evolving GL and calving front. The hybrid shallow approximation of Stokes flow allows for large-scale, long-term simulations of ice-sheet evolution. Unless otherwise stated, we used surface temperature anomalies from the WAIS divide ice-core (WDC) reconstruction[61], which show a sharp increase of 11 K starting around 17 kyr BP. For surface accumulation we use the 1980-2000 mean accumulation from the output of a regional climate model (RACMOv2.1, HadCM3, ref. 62) as a base accumulation pattern and scale this pattern by 2% per degree of climatic temperature change from present[63] (using the WDC reconstruction) and by 43% per km surface elevation change. The latter assumes a linear dependence of air temperature on elevation combined with an exponential dependence of precipitation on temperature. At the ice-ocean interface we use the Potsdam Ice-shelf Cavity mOdel (PICO)[64], which calculates melt patterns underneath the ice shelves for given ocean conditions[65]. Ocean temperature anomalies are computed from ice-core derived surface temperature anomalies convolved with a response function to produce a damped and delayed response[66]. The calving front can freely evolve with calving parameterized to be dependent on principal strain rates at the ice-shelf front[67]. Basal sliding is parameterized using an iterative optimization scheme[68] modified for the till-friction angle, mimicking the distribution of marine sediment and bedrock, such that the mismatch to modern surface elevation observations is minimized.

Sea-level change drives GL migration through the flotation criterion, which determines GL position[69]. We prescribe sea-level changes by considering the height of the sea surface and the height of the sea floor separately. Unless otherwise stated, we use global mean sea surface heights prescribed by the ICE-6G GIA model[70]. According to this model, mean sea-surface height has risen by about 100 m since 14.5 kyr BP. Alternative sea-surface height records were considered as part of the sensitivity analysis discussed below.

Changes to the height of the sea floor and bed topography are modelled using an approach that reflects the deformation of an elastic plate overlying a viscous half-space. Calculations are carried out using the computationally efficient Fast Fourier Transform to solve the biharmonic differential equation for vertical displacement in response to ice load change[71]. This approach can also be used to calculate vertical displacement in response to spatially-varying water load changes (more details below). A key advantage this approach has over traditional Elastic Lithosphere Relaxing Asthenosphere (ELRA) models is that the response time of the sea floor is not considered a constant, but depends on the wavelength of the ice-load perturbation. This formulation closely approximates the approach used within many GIA models [71]. Since our ice-sheet model is not coupled to a GIA model we are unable to prescribe self-consistent water load changes or account for feedbacks associated with post-glacial changes to the rotational state of the Earth[72]. The effect of neglecting these processes is discussed below in the section on sea-level forcing.

Bed elevation adjustment

With a resolution of 15 km and uncertain bed elevation, basal conditions and climate forcings, matching the present-day GL position in the Weddell Sea required raising the ice-sheet bed in one key location (Bungenstock Ice Rise) to compensate for topographic information lost during remapping.

The present-day elevations of the sea bed and ice-sheet bed are regionally highly uncertain[30,73]. Furthermore, when remapping observed bed elevations (Bedmap2; ref. 30) from a relatively fine spatial grid (1 km) to the spatial resolution of our simulations (15 km), we lose bed-elevation information in key places. Remapping introduces inherent uncertainty into any low-resolution ice-sheet modelling study, but it is particularly important for the process of ice rise re-grounding that we highlight. For example, at present-day ice rises the remapping of the bed elevation data reduces the apparent peak bed elevation by 36-135 m, while at their steep flanks this difference can be a few hundred meters (Extended Data Fig. 4). We find that in our simulations, if we use bed topography remapped directly from the Bedmap2 compilation, (using a first-order conservative technique[74]), the GL in the Weddell Sea Sector does not re-advance across a 1.300m-deep trough and often remains near to its Holocene minimum position, far inland of its present-day location, until the end of simulations. This is unrealistic.

We have experimented with various approaches to dealing with the uncertainty introduced by remapping bed topography to lower spatial resolutions. These include adopting the maximum Bedmap2 value in each model gridcell either in the regions of individual ice rises or across the whole ice sheet. We also experimented with a sub-grid pinning point scheme, dependent on the thickness of the water column underneath the ice shelf within some uncertainty range[75] and with a simpler uniform adjustment in the region of individual ice rises. Which approach we take affects the timing and magnitude of GL retreat and re-advance. Without clear motivation to adopt a more complex approach, we made the minimum adjustment to the bed that allowed the

GL to re-advance in the Weddell Sea Sector: we uniformly raised the bed by 150 m in a 165 km by 180 km area centered on Bungenstock Ice Rise (BIR) only. This rather arbitrary choice is a major limitation of this model ensemble, which prevents us (along with other uncertainties associated with model resolution, forcings, parameters and physics, see below) from extracting information about the timing of GL retreat and re-advance from our simulations.

The purpose of our model experiments is to explore the mechanisms that could have caused re-advance and what impacts these mechanisms. It is beyond our scope to explore the range of options to compensate for basal topographic re-mapping errors, but our work highlights that, at least for studying ice-rise re-grounding, resolving this issue will be required if we are to make quantitative predictions of millennial-scale ice sheet behavior.

Model ensemble and the reference simulation

We performed an ensemble of simulations, each spanning 205 kyr BP to present, in which uncertain parameters were systematically varied and the results were compared to paleo-ice-sheet datasets and present-day observations[76,77]. The full results of the ensemble represent a likely range of Antarctic ice-sheet chronologies and will be presented elsewhere. Here we are focused on the possible extent and triggers of large-scale GL re-advance during the Holocene and so only discuss in detail mechanisms relevant to this process. We choose one of the ensemble members to act as a reference simulation to demonstrate aspects of model behavior. The reference simulation is chosen from many ensemble members that employ parameters that lie within physically-plausible bounds (Extended Data Table 2) and also achieve reasonable agreement with a commonly-used ice-sheet GL position reconstruction[2]. Despite this GL reconstruction not including GL re-advance during the Holocene, as discussed in the main text, many ensemble members, including our reference simulation, simulate the GL retreating significantly inland of its present-day position and subsequently re-advancing towards it current position. We express ice-mass changes as the above-flotation volume in units of global sea-level equivalent, assuming a constant ocean area of 3.61×10^{14} m^2 (ref. 78).

The drivers of GL re-advance

We performed three model experiments (separate from the full ensemble, above) to disentangle the causes of re-advance in the Weddell and Ross Sea sectors. We find that both uplift of the bed at the GL and buttressing caused by the formation of ice rises drive re-advance of the GL towards its present-day position in both the sectors (Extended Data Fig. 4). The first experiment ('No uplift'; Extended Data Fig. 4) is identical to the reference simulation except that uplift is halted after 10 kyr BP, i.e. at approximately the time at which the GL in the reference simulation reaches its most retreated position in both sectors (Fig. 3). The GL in the Weddell Sea remains at its 10 kyr BP position for the remainder of the simulation. In the Ross Sea the GL retreats further into the interior of the ice sheet. This additional retreat can be prevented by buttressing, as demonstrated in the second experiment ('No uplift, grounding of ice rises'; Extended Data Fig. 4), where uplift is again halted 10 kyr BP, but ice-rise formation is enforced by raising the seafloor in the locations of the Crary, Steershead, Henry and Korff ice rises and Doake Ice Rumples. In this simulation further retreat in the Ross Sea is prevented, but re-advance still does not occur in either sector. We further test the relevance of buttressing via ice-rise formation in a third experiment ('Uplift, no grounding of ice rises'; Extended Data Fig. 4) in which uplift of the bed is allowed, but ice-rise formation is prevented by lowering the seafloor. In this simulation ice-shelf buttressing is reduced compared to the reference simulation. Consequently, the GL remains at its 10 kyr BP position in the Weddell Sea (Extended Data Fig. 4a) and relatively little re-advance occurs in the Ross Sea (Extended Data Fig. 4b). Hence we identify the grounding of HIR, as evident from our radar survey, as critical for GL re-advance in the Weddell Sea in these simulations, while in the Ross Sea neither uplift in the GL region nor buttressing due to ice-rise formation, is alone sufficient to drive GL re-advance to the present-day position.

Model sensitivity to forcings

Extended Data Fig. 6 plots selected results from our analysis of the sensitivity of the model to various forcings. The retreat of the GL inland of its present-day location and subsequent re-advance is a common behaviour of the model, however the Holocene minimum extent, and how fast and how far the GL re-advances are all sensitive to forcings.

Since **sea-level forcing** is highly relevant for deglaciation, the responses to four different eustatic sea-level reconstructions were compared (Extended Data Fig. 6a). In our reference simulation we use the sea-level curve from the ICE-6G model[70]. Ref. 79 and ref. 80 provide similar sea-level reconstructions and hence similar model results, with the strongest changes after around 15 kyr BP. The SPECMAP timeseries[81] was used in the SeaRISE intercomparison[78] and shows a delayed LGM sea-level lowstand as well as a delayed sea-level rise to Holocene conditions and hence the modelled ice sheet exhibits a later retreat and re-advance (Extended Data Fig. 6).

In order to mimic the first-order effects of GIA coupling[82] (including rotational feedback and self-gravitational effects) we experimented with scaling the sea-level forcing time-series by factors of 0.9 and 0.8 (initiated at 35 kyr BP, Extended Data Fig. 6b). We do not attempt to prescribe spatially-varying sea-level forcing, but comparison with independent GIA model output[83] suggests that neglect of rotational feedback and self-gravitation of the ocean may result in local errors in sea-level forcing on the order of 15-20 m (this range reflects the likely error associated with prescribing sea surface height; deformation of the seabed is self-consistently modeled within PISM). Scaling the uniform sea-level forcing by a factor of 0.9 causes the lowstand to be less pronounced at the LGM (approximately 10 m higher), in comparison to the reference simulation. This affects the LGM GL position, particularly in the Ross Sea, which in turn affects the retreat and re-advance of the GL, because the depression of the bed depends sensitively on the ice-sheet's LGM extent. Scaling by 0.8 may be unrealistic (based on comparison with GIA model output generated using an independent ice-sheet history[83]; results not shown), and interestingly, we note that retreat behind the present-day GL position is not reproduced in this scenario (Extended Data Fig. 6b). We also experiment with a sea-level forcing that is identical to that used in the reference simulation (ICE-6G model[70]) except that the curve has been uniformly shifted 2 kyr earlier. The result is that the GL responds with an earlier retreat. This response emphasizes the key role of the sea-level forcing in triggering large-scale GL retreat.

Sea-level changes also impact the load of the ocean on the sea bed. This triggers bed deformation, which will affect GL migration. By default, this second-order effect is not accounted for in PISM. However, we carried out exploratory simulations that do account for it (not shown), and find that when GL retreat is accompanied by an increase in eustatic sea-level, the additional ocean load partly counteracts the unloading associated with GL retreat. Accordingly, the GL retreats further inland than in the reference simulation. On the other hand, sea bed uplift following GL retreat reduces the water load in marine sectors, this further amplifies uplift, which supports GL advance. These interesting second-order effects do not qualitatively affect model behavior, but they do impact the magnitude of GL retreat and re-advance via their influence on LGM extent in both the Weddell and Ross sectors.

For surface **temperature forcing** our reference simulation uses a reconstruction of the WAIS divide ice core (WDC)[61]. The results are similar when an alternative reconstruction from the EPICA Dome C ice core (EDC)[84] is used (Extended Data Fig. 6c). However, the GL responds to the slightly warmer LGM conditions in the EDC case with less LGM advance and hence a less severe retreat in the Ross Sea Sector. For comparison, we also force one simulation with a temperature record pertaining to the start of the Last Interglacial Period (from the EDC core), in which an earlier and stronger warming leads to an earlier and stronger GL retreat, particularly in the Ross Sea Sector.

Accumulation in the reference simulation is coupled to changes in surface temperature by imposing a 2% precipitation change for each degree variation from present-day temperatures (Extended Data Fig. 6d, violet curves) due to climatic changes (constrained by ice core data) and a 43% precipitation per km of surface elevation change. We experimented with two alternative time-dependent accumulation forcings and two constant accumulation scenarios. Using either a scaling of 5% per degree of WDC-temperature change or an independent WDC-derived accumulation reconstruction[85] leads to lower mean accumulation and a less advanced LGM GL position(Extended Data Fig. 6d). The less advanced LGM GL almost eliminates GL retreat inland of its present position and re-advance, particularly in the Weddell Sea. When accumulation is kept constant at LGM conditions (2% per degree scaling of the EDC temperature at 25 kyr BP; Extended Data Fig. 6d), which correspond to lower accumulation than today, the GL retreats inland of its present-day location in both sectors, but only partially re-advances in the Ross Sea and does not re-advance in the Weddell Sea. When accumulation is kept constant at present-day values (Extended Data Fig. 6d) GL retreat starts earlier than in the reference simulation, particularly in the Ross Sea. In both sectors the GL retreats and re-advances in a similar way to the reference simulation, but with different timings: in the Weddell Sea the GL re-advances several thousand years earlier than in the reference simulations, while in the Ross Sea re-advance is delayed in comparison to the reference simulation.

Model sensitivity to parameters

Next we use selected members of the ice-sheet model ensemble to demonstrate the sensitivity of the model to various parameter values. Analysis of the full model ensemble, including a systematic validation of the full range of parameter combinations against present-day conditions and reconstructions of paleo conditions[28,77], will be presented elsewhere. Here we present the impact of single parameter perturbations. In general, we find that retreat of the GL inland of its present-day location and subsequent re-advance occurs over a wide range of parameter choices, but the Holocene minimum extent, and how fast and how far the GL re-advances are all sensitive to these choices.

Mantle viscosity affects model behavior because it defines the rate and pattern of the deformation of the ice-sheet bed and sea floor. Our reference simulation uses a mantle viscosity of $5\text{x}10^{20}$ Pa s. The ensemble also covered a value considered typical for pan-Antarctic model simulations and used as the default value in PISM ($1\text{x}10^{21}$ Pa s; Extended Data Fig. **7**a). We selected the lower value for our reference simulation to account for the weaker mantle beneath the WAIS[86]. An even lower viscosity ($\sim1\text{x}10^{20}$ Pa s; Extended Data Fig. **7**a) has also been tested. In the lowest viscosity case, GL retreat inland of the present-day position is prevented as the bed responds too quickly to ice unloading. We find the fastest GL retreat rates for higher viscosities. The most inland position reached by the GL is similar in each case, except the lowest viscosity case, and re-advance occurs earlier for lower mantle viscosity. In summary, we find that GL retreat and re-advance occurs in a plausible but confined range of mantle viscosity values.

Flexural rigidity is associated with the thickness of the elastic lithosphere and has an influence on the horizontal extent to which bed deformation responds to changes in load. Previous studies based on gravity modeling suggest appropriate values for our study with a focus on West

Antarctica lying within the range of $5x10^{23}$ to $5x10^{24}$ N m (refs. 87, 88). Our reference simulation marks the upper end of this range (Extended Data Fig. 7a). For lower values, $1x10^{24}$ to $5x10^{23}$ N m, we find GL retreat beyond its present-day location and re-advance as in the reference simulation. However maximum retreat is delayed in the Ross Sea sector, so re-advance of the GL does not reach its present-day location in that sector.

Enhancement factors are used in ice modeling to account for anisotropy and other unresolved rheological properties. PISM employs one enhancement factor for the shallow-shelf approximation (SSA) component of the constitutive law and a second enhancement factor for the shallow-ice approximation component. Increasing the SSA-enhancement factor (Extended Data Fig. 7b) and/or decreasing the SIA-enhancement factor (Extended Data Fig. 7c) produces a less advanced LGM GL position. This is because larger values of the SSA-enhancement factor produce faster ice streams and thinner ice shelves, and smaller values of the SIA-enhancement factor produce thicker grounded ice. For a less advanced LGM GL, retreat initiates earlier and progresses more slowly, and does not reach as far inland before retreat is halted.

PISM uses a generalized sliding parameterization formulated as an exponential sliding law[60]. In the reference simulation we use a **sliding exponent**, $q = 0.75$ (Extended Data Fig. 7d). In the plastic case ($q = 1$), the LGM GL is less advanced and retreat starts earlier (Extended Data Fig. 7d). For smaller values of q retreat occurs generally later in the Weddell Sea and retreat in the Ross Sea is less pronounced.

Two other parameters associated with the sliding parameterization are the **decay rate of till water** and the **effective overburden pressure**[60]. Within the range explored by the ensemble, both parameters have only a moderate effect on LGM GL extent and the timing of retreat, and do not affect whether or not the GL retreats inland of its present-day location and re-advances

(Extended Data Fig. 7e).

A final sliding-related parameter is the **till friction angle**, which varies spatially and for our reference simulation is optimized[68] to minimize the mismatch between modelled and observed surface elevation, but is constrained to be larger than 2°. Reducing the minimum value to 1° leads to a smaller LGM extent and hence a slower retreat and larger minimum extent (preventing retreat past the present-day GL position in the Weddell Sea) (Extended Data Fig. 7f). Instead of optimizing the till friction angle using observed surface elevations, it can also be defined as a linear piece-wise function of bed topography, with 2° used in areas below -500 m (this is the default approach in PISM)[60]. This also reduces the LGM extent and, in the Ross Sea, reduces the retreat of the GL inland of its present-day extent.

Ocean forcing in our simulations is modelled with PICO[64]. PICO employs parameters for **overturning strength** and **heat exchange**. Modification of the parameter values affects the LGM GL extent and hence the rate and timing of retreat (Extended Data Fig. 7g). However, GL retreat and re-advance are produced as robust features for extreme parameter values, even if melting is omitted or prescribed as a constant at present-day values.

Calving is parameterized as **eigencalving** (dependent on strain rates)[67]. A parameter K is the constant of proportionality between calving rate and horizontal spreading rate of ice shelves(Extended Data Fig. 7h). K is assumed constant and uniform. Our reference simulation uses $K = 1\text{x}10^{17}$ m s. LGM GL position is less advanced for smaller eigencalving values, and GL retreat less pronounced, likely due to additional ice-shelf buttressing resulting from less calving.

Resolution dependence

Our simulations, in common with all millennial-timescale ice-sheet simulations, suffer from significant limitations related to the maximum practical spatial resolution that they can employ.

Just like the model parameters considered in the previous section, the spatial resolution can be treated as a quantity that affects the results of the simulations and should be investigated. This is particularly true in our study as ice-shelf grounding on bathymetric highs with relatively small horizontal dimensions has proven to be so important for the large-scale evolution of the ice sheet.

A sensitivity analysis aimed at examining the sensitivity of this behavior to resolution (analogous to the exercise described above) is highly limited by computational resources. For example, doubling the spatial resolution incurs at least a ten-fold increase in computational cost. Ensembles with systematically-varied parameters of simulations that span the full spin-up over two glacial cycles (205 kyr) currently are only possible with a spatial resolution of 15 km.

Shorter duration simulations (that only cover the last 20 kyr) are possible using a resolution of up to 7 km, if they are initiated at 20 kyr BP by remapping the spun-up state of a 15 km resolution simulation. (Unfortunately, this remapping means that, despite higher resolution, the bed topography is no better resolved with respect to observations[30] than the 15 km resolution simulations.) Higher resolution simulations generally reproduce the pattern of GL retreat and re-advance, but the increase in resolution strongly impacts the timing and magnitude of changes (Extended Data Fig. 8). Due to the influence of resolution on other model parameters, a full ensemble analysis at higher resolution would be required to fully characterize the resolution dependence of our simulations. Furthermore, these simulations would need to use the higher resolution throughout the 205 kyr spin-up period in order to benefit from better-resolved bed topography. This is unfeasible with currently-available computing resources.

Geophysical and terrestrial evidence consistent with re-advance.

Previous geophysical and terrestrial observations are consistent with our proposed sequence of retreat and re-advance, but do not yet provide a coherent pattern of retreat and re-advance. Their spatial coverage is currently insufficient to reveal the full complexity of Holocene retreat and re-advance. In the Weddell Sea, ref. 55 presented evidence that Korff Ice Rise (KIR; Fig. 1) has been in a steady configuration since around 2.5 kyr BP. However, prior to that time KIR could have undergone significant flow disturbance, including near-complete ungrounding and regrounding (as occurs in our reference simulation; Supplementary Video 1), if subsequent steady ice flow has had sufficient time to remove englacial evidence of such a flow disturbance. See ref. 55 for details of this interpretation. Radar over Bungenstock Ice Rise (BIR; Fig. 1) suggests a reorganization in flow as early as 4 kyr BP (ref. 89), while regional uplift rates suggest that BIR may have been ungrounded between 4-2 kyr BP (ref. 5). In the Ellsworth[90] and Pensacola Mountains[91,92], exposure dates do not provide evidence for, but are consistent with thinning below present and re-thickening within the last ~4 kyr (ref. 93). Ref. 94 noted that radar-derived basal topography upstream of a subglacial basin beneath the Institute and Möller ice streams suggests a former GL position more than 100 km upstream of today's grounding line, although they did not suggest that this was a Holocene GL position.

Similarly, in the Ross Sea exposure-age dating in the Trans-Antarctic Mountains (e.g. ref. 3,4, 43, 95) may be consistent with our conclusions, but cannot confirm or rule-out re-advance. Geophysical observations have hinted at recent re-advance. Borehole temperatures have been used to date the grounding and formation of Crary Ice Rise (CIR; Fig. 1b) to 1.5-1.0 kyr BP (ref. 58) and ice-penetrating radar surveys of Kamb Ice Stream indicates that the GL was upstream of its current location during the last few centuries[9]. However, it is unclear if the latter observation is evidence for a long-term large-scale re-advance, or for relatively-small-scale GL fluctuations.

In both sectors, it is unclear if these varied observations from diverse glacial environments (outlet glaciers, ice streams, ice rises, nunataks), paint a consistent picture of the timing of retreat and re-advance. Our work does not provide any detailed timing constraints; the timing of simulated GL migration depends on uncertain bed topography and model parameters, and further work is needed to extract timing information from our radiocarbon and radar observations. We leave to future work the important task of unravelling a retreat-readvance chronology consistent with all observations.

Code Availability

PISM code used in this study can be obtained from https://doi.org/10.5281/zenodo.1199066. Results and plotting scripts are available from the authors on request. Scripts for processing and plotting radar data are also available on request.

Data Availability

Ice-penetrating radar data can be obtained from the UK Polar Data Centre: http://doi.org/99d. A simple MATLAB script for viewing the raw radar data is also provided at this link. The radiocarbon data supporting the findings of this study are available in Extended Data Table 1.

References

[30] Fretwell, P. Pritchard, H. D. Vaughan, D. G. et al. Bedmap2: improved ice bed, surface and thickness datasets for Antarctica *The Cryosphere* **7,** (2013).

[31] Rignot, E. Mouginot, J. & Scheuchl, B. Ice flow of the Antarctic ice sheet *Science* **333,** 1427–1430 (2011).

[32] Depoorter, M. A. Bamber, J. Griggs, J. et al. Calving fluxes and basal melt rates of Antarctic ice shelves. *Nature* **502,** 89 (2013).

[33] Lipps, J. H. Ronan, T. & DeLaca, T. Life below the Ross ice shelf, Antarctica. *Science* **203,** 447–449 (1979).

[34] Haran, T., Bohlander, J., Scambos, T. et al. MODIS Mosaic of Antarctica 2003-2004 (MOA2004) Image Map. Boulder, Colorado USA: National Snow and Ice Data Center. http://dx.doi.org/10.7265/N5ZK5DM5. (2005)

[35] Scambos, T., T. Haran, M. Fahnestock, T. Painter, and J. Bohlander. 2007. MODIS-based Mosaic of Antarctica (MOA) Data Sets: Continent-wide Surface Morphology and Snow Grain Size. Remote Sensing of Environment 111(2): 242-257. http://dx.doi.org/10.1016/j.rse.2006.12.020.

[36] Scherer, R. P. Quaternary and tertiary microfossils from beneath ice stream B: evidence for a dynamic West Antarctic ice sheet history. *Palaeogeogr. Palaeoclimatol. Palaeoecol.* **90,** 395–412 (1991).

[37] Coenen, J.J., Inferring West Antarctic subglacial basin history and ice stream processes using siliceous microfossils. *M.S. Thesis*, Northern Illinois University, DeKalb, IL, (2016)

[38] Scherer, R. P. Aldahan, A. Tulaczyk, S. et al. Pleistocene collapse of the West Antarctic ice sheet. *Science* **281,** 82–85 (1998).

[39] Abbott, M. B. & Stafford Jr, T. W. Radiocarbon geochemistry of modern and ancient Arctic lake systems, Baffin Island, Canada *Quat. Res.* **45,** 300–311 (1996).

[40] Priscu, J.C., Achberger, A.M., Cahoon, J.E., Christner, B.C., Edwards, R.L., Jones, W.L., Michaud, A.B., Siegfried, M.R., Skidmore, M.L., Spigel, R.H. and Switzer, G.W., 2013. A microbiologically clean strategy for access to the Whillans Ice Stream subglacial environment. *Antarctic Science*, *25*(5), pp.637-647.

[41] Rosenheim, B. E. Santoro, J. A. Gunter, M. et al. Improving Antarctic sediment 14 C dating using ramped pyrolysis: An example from the Hugo Island trough. *Radiocarbon* **55,** 115–126 (2013).
[42] Clark, P. U. Dyke, A. S. Shakun, J. D. et al. The last glacial maximum. *Science* **325,** 710–714 (2009).
[43] Anderson, J. B. Conway, H. Bart, P. J. et al. Ross Sea paleo-ice sheet drainage and deglacial history during and since the LGM. *Quat. Sci. Rev.* **100,** 31–54 (2014).
[44] Andrews, J. T. Domack, E. W. Cunningham, W. L. et al. Problems and possible solutions concerning radiocarbon dating of surface marine sediments, Ross Sea, Antarctica. *Quaternary Research* **52,** 206–216 (1999).
[45] Licht, K. J. & Andrews, J. T. The 14 C record of Late Pleistocene ice advance and retreat in the central Ross Sea, Antarctica. *Arctic, Antarctic, and Alpine Research* 324–333 (2002).
[46] McKay, R. Dunbar, G. Naish, T. et al. Retreat history of the Ross Ice Sheet (Shelf) since the Last Glacial Maximum from deep-basin sediment cores around Ross Island. *Palaeogeogr. Palaeoclimatol. Palaeoecol.* **260,** 245–261 (2008).
[47] Martinerie, P. Raynaud, D. Etheridge, D. M. et al. Physical and climatic parameters which influence the air content in polar ice. *Earth Planet. Sci. Lett.* **112,** 1–13 (1992).
[48] Federer, U. Kaufmann, P. R. Hutterli, M. A. et al. Continuous flow analysis of total organic carbon in polar ice cores. *Environmental science & technology* **42,** 8039–8043 (2008).
[49] Antony, R. Mahalinganathan, K. Thamban, M. et al. Organic carbon in Antarctic snow: spatial trends and possible sources. *Environ. Sci. Technol.* **45,** 9944–9950 (2011).
[50] Joughin, I. Tulaczyk, S. MacAyeal, D. R. et al. Melting and freezing beneath the Ross ice streams, Antarctica. *J. Glaciol.* **50,** 96–108 (2004).
[51] Tulaczyk, S., Kamb, B. and Engelhardt, H.F. Estimates of effective stress beneath a modern West Antarctic ice stream from till preconsolidation and void ratio. *Boreas* **30**(2), 101–114 (2001)
[52] Christianson, K. Jacobel, R. W. Horgan, H. J. et al. Basal conditions at the grounding zone of Whillans Ice Stream, West Antarctica, from ice-penetrating radar. *J. Geophys. Res. Earth Surf.* **121,** 1954–1983 (2016).
[53] Hall, B. L. Henderson, G. M. Baroni, C. et al. Constant Holocene Southern-Ocean 14 C reservoir ages and ice-shelf flow rates. *Earth Planet. Sci. Lett.* **296,** 115–123 (2010).
[54] Van Liefferinge, B. & Pattyn, F. Using ice-flow models to evaluate potential sites of million year-old ice in Antarctica. *Clim. Past* **9,** 2335 (2013).
[55] Kingslake, J. Martín, C. Arthern, R. J. et al. Ice-flow reorganization in West Antarctica 2.5 kyr ago dated using radar-derived englacial flow velocities. *Geophys. Res. Lett.* **43,** 9103–9112 (2016).
[56] Ely, J. Clark, C. Ng, F. et al. Insights on the formation of longitudinal surface structures on ice sheets from analysis of their spacing, spatial distribution, and relationship to ice thickness and flow. *J. Geophys. Res. Earth Surf.* **122**, 961–972 (2017).
[57] Favier, L. & Pattyn, F. Antarctic ice rise formation, evolution, and stability. Geophys. Res. Lett. **42**(11), 4456-4463 (2015).
[58] Bindschadler R. A., Roberts E. P. & Iken A. Age of Crary Ice Rise, Antarctica, determined from temperature-depth profiles. *Ann. Glaciol.* **14,** 13–16 (1990).
[59] Bueler, E. & Brown, J. Shallow shelf approximation as a "sliding law" in a thermomechanically coupled ice sheet model. *J. Geophys. Res. Earth Surf.* **114,** (2009).
[60] The PISM authors. PISM, a Parallel Ice Sheet Model: User's Manual (2016), based on development revision e9d2d1f8 (March 7th, 2017).
[61] Cuffey, K. M. Clow, G. D. Steig, E. J. et al. Deglacial temperature history of West Antarctica. *Proceedings of the National Academy of Sciences* **113,** 14249–14254 (2016).
[62] Ligtenberg, S. van de Berg, W. van den Broeke, M. et al. Future surface mass balance of the Antarctic ice sheet and its influence on sea level change, simulated by a regional atmospheric climate model. *Clim Dyn* **41,** 867–884 (2013).
[63] Frieler, K. Clark, P. U. He, F. et al. Consistent evidence of increasing Antarctic accumulation with warming *Nature Climate Change* **5,** 348–352 (2015).
[64] Reese, R., Albrecht, T., Mengel, M. et al. Antarctic sub-shelf melt rates via PICO. *Cryosphere Discuss.* **2017,** 1–24 (2017).
[65] Schmidtko, S. Heywood, K. J., Thompson, A. F. et al. Multidecadal warming of Antarctic waters *Science* **346,** 1227–1231 (2014).
[66] Li, C., von Storch, J. S., & Marotzke, J. Deep-ocean heat uptake and equilibrium climate response. *Climate Dynamics*, **40**, 1071-1086 (2015).
[67] Levermann, A. Albrecht, T. Winkelmann, R. et al. Kinematic first-order calving law implies potential for abrupt ice-shelf retreat *The Cryosphere* **6,** 273 (2012).
[68] Pollard, D. & DeConto, R. A. simple inverse method for the distribution of basal sliding coefficients under ice sheets, applied to Antarctica *The Cryosphere* **6,** 953 (2012).
[69] Feldmann, J., Albrecht, T. Khroulev, C. et al. Resolution-dependent performance of grounding line motion in a shallow model compared with a full-Stokes model according to the MISMIP3d intercomparison. *J. Glaciol.* **60,** 353–360 (2014)..
[70] Stuhne, G. & Peltier, W. Reconciling the ICE-6G_C reconstruction of glacial chronology with ice sheet dynamics: The cases of Greenland and Antarctica. *J. Geophys. Res. Earth Surf.* **120,** 1841–1865 (2015).
[71] Bueler, E., Lingle, C. S. & Brown, J. Fast computation of a viscoelastic deformable Earth model for ice-sheet simulations *Ann. Glaciol.* **46,** 97–105 (2007).
[72] Milne, G., Mitrovica, J. X. & Davis, J. L. Near-field hydro-isostasy: the implementation of a revised sea-level equation. *Geophys. J. Int.*, **139**, 464-482 (1999).
[73] Pritchard, H. D. Bedgap: where next for Antarctic subglacial mapping? *Antarctic Science* **26,** 742–757 (2014).
[74] Jones, P.W. Monthly Weather Review, 127, 2204-2210 (1999).
[75] Pollard, D. and DeConto, R.M., 2012. Description of a hybrid ice sheet-shelf model, and application to Antarctica. Geoscientific Model Development, 5(5), p.1273.
[76] Briggs, R. D. Pollard, D. & Tarasov, L. A data-constrained large ensemble analysis of Antarctic evolution since the Eemian. *Quat. Sci. Rev.* **103,** 91–115 (2014).
[77] Pollard, D., Chang, W., Haran, M., Applegate, P. and DeConto, R. Large ensemble modeling of the last deglacial retreat of the West Antarctic Ice Sheet: comparison of simple and advanced statistical techniques. *Geosci. Mod. Dev.*, **9**(5) (2016)
[78] Bindschadler, R. A. Nowicki, S. Abe-Ouchi, A. et al. Ice-sheet model sensitivities to environmental forcing and their use in projecting future sea level (the SeaRISE project). *J. Glaciol.* **59,** 195–224 (2013).
[79] Lambeck, K. Rouby, H. Purcell, A. et al. Sea level and global ice volumes from the Last Glacial Maximum to the Holocene. *Proceedings of the National Academy of Sciences* **111,** 15296–15303 (2014).
[80] Bintanja, R. & Van de Wal, R. North American ice-sheet dynamics and the onset of 100,000-year glacial cycles. *Nature* **454,** 869 (2008).

[81] Imbrie, J. D. & McIntyre, A. SPECMAP time scale developed by Imbrie et al., 1984 based on normalized planktonic records (normalized O-18 vs time, specmap.017) – (2006).
[82] Gomez, N. Pollard, D. & Mitrovica, J. X. A 3-D coupled ice sheet–sea level model applied to Antarctica through the last 40 ky. *Earth Planet. Sci. Lett.* **384,** 88–99 (2013).
[83] Whitehouse, P. L., Bentley, M. J., Milne, G. A., King, M. A., & Thomas, I. D. A new glacial isostatic model for Antarctica: calibrated and tested using observations of relative sea-level change and present-day uplift rates. *Geophys. J. Int.* **190**, 1464-1482 (2012).
[84] Jouzel, J. Masson-Delmotte, V. Cattani, O. et al. Orbital and millennial Antarctic climate variability over the past 800,000 years. *Science* **317,** 793–796 (2007).
[85] Fudge, T. Markle, B. R. Cuffey, K. M. et al. Variable relationship between accumulation and temperature in West Antarctica for the past 31,000 years. *Geophys. Res. Lett.* **43,** 3795–3803 (2016).
[86] Hay, C.C., Lau, H.C., Gomez, N., Austermann, J., Powell, E., Mitrovica, J.X., Latychev, K. and Wiens, D.A. Sea Level Fingerprints in a Region of Complex Earth Structure: The Case of WAIS. *Journal of Climate*, *30*(6), 1881-1892 (2017)
[87] Ji, F., Gao, J., Li, F., Shen, Z., Zhang, Q. and Li, Y., Variations of the effective elastic thickness over the Ross Sea and Transantarctic Mountains and implications for their structure and tectonics. Tectonophysics, 717, (2017).
[88] Chen, B., Haeger, C., Kaban, M.K. and Petrunin, A.G., 2017. Variations of the effective elastic thickness reveal tectonic fragmentation of the Antarctic lithosphere. Tectonophysics, *in press*.
[89] Siegert, M. Ross, N. Corr, H. et al. Late Holocene ice-flow reconfiguration in the Weddell Sea sector of West Antarctica. *Quat. Sci. Rev.* **78,** 98–107 (2013).
[90] Hein A. S. et al. Mid-Holocene pulse of thinning in the Weddell Sea sector of the West Antarctic ice sheet. *Nat. Commun.* **7,** (2016).
[91] Balco G. et al. Cosmogenic-nuclide exposure ages from the Pensacola Mountains adjacent to the Foundation Ice Stream, Antarctica. *Am. J. Sci.* **316,** 542–577 (2016).
[92] Bentley M. J. et al. Deglacial history of the Pensacola Mountains, Antarctica from glacial geomorphology and cosmogenic nuclide surface exposure dating. *Quat. Sci. Rev.* **158,** 58–76 (2017).
[93] Whitehouse P. L. et al. Controls on Last Glacial Maximum ice extent in the Weddell Sea embayment, Antarctica. Journal of Geophysical Research: Earth Surface. *J. Geophys. Res. Earth Surf.* **122,** 371–397 (2017).
[94] Ross, N., Bingham, R.G., Corr, H.F., Ferraccioli, F., Jordan, T.A., Le Brocq, A., Rippin, D.M., Young, D., Blankenship, D.D. and Siegert, M.J. Steep reverse bed slope at the grounding line of the Weddell Sea sector in West Antarctica. *Nature Geoscience*, **5**(6), 393 (2012).
[95] Todd C., Stone J., Conway H., Hall B. & Bromley G. Late Quaternary evolution of Reedy Glacier, Antarctica. *Quat. Sci. Rev.* **29,** 1328–1341 (2010).

Extended Data Captions

Extended Data Figure 1: Crevassing at Doake Ice Rumples. a, Radarsat Antarctic Mapping Project (RAMP)[96] image showing the surface expression of ice-shelf crevasses in synthetic aperture radar data. Light areas indicate high backscatter from (near)surface reflectors interpreted to be surface crevasses. Crevasses form over and immediately downstream of Doake Ice Rumples. We hypothesize that crevasses once formed in a similar manner over the topographic high beneath the northern tip of HIR. **b,** Close-up view of the crevasses (black box in **a** shows location), whose spacing (100-300 m), orientation (perpendicular to the flow of the ice shelf) and lateral extent (~10 km) are similar to the steeply-dipping reflectors discovered near the bed of the northern tip of HIR (e.g. Extended Data Fig. 2g) in the region of a topographic high. Yellow curves are flow lines computed from satellite-derived surface velocities[31]. Flow is from bottom to top. Polar stereographic coordinates are in km. The present-day GL[32] is in red.

Extended Data Figure 2: Relic crevasses in Henry Ice Rise. a, Radargram aligned perpendicular to the divide ridge (inset shows location). One undulating isochrone is highlighted. The colours show normalised elevation. **b** and **c,** close-up views of the regions indicated in **a** by the boxes. In both close-up panels, diffractors (hyperbolic reflectors) are interpreted as expressions of relic crevasses (data is unmigrated). The red vertical dashed line in **c** is the present-day GL[32]. **d**, **e** and **f,** Radargrams aligned approximately perpendicular to northern relic crevasses (**d** and **e** show migrated data). In **c** ($6 \leq x \leq 8$ km) and **f** ($0.3 \leq x \leq 1.4$ km) isochrones intercepting the bed are evident. **g,** Three relic crevasses mapped across several radar lines over a RAMP image[96]. Inset shows an oblique, three-dimensional view of the features over an interpolated surface showing the bed elevation z_b (Methods). Crevasse spacing in these areas ranges between approximately 200 m and 600 m. The arrow indicates the view direction of the oblique view.

Extended Data Figure 3: Grounding-line retreat and lithospheric rebound. Cross-sections along transects through the Weddell (left) and Ross (right) Sea sectors, at 5 kyr intervals (for transects see Fig. 3). Horizontal axis shows distance from the present-day GL. Vertical blue dashed line shows position of maximum GL retreat. **a** and **b,** 15 kyr BP, with GL close to the continental shelf edge. **c** and **d,** 10 kyr BP, GL retreat to approximately its minimum, most retreated location. **e** and **f,** 5 kyr BP**,** both ice shelves have grounded on sub-ice-shelf bathymetric highs due to seafloor uplift. **g** and **h,** Present day, the GL has re-advanced to approximately the present-day configuration in response to the grounding of the ice shelf and uplift at the GL. The Crary (CIR), Bungenstock (BIR) and Henry (HIR) ice rises are labelled in **g** and **h**. The Whillans Ice Stream (WIS) and Subglacial Lake Whillans (SLW) sediment core locations are labelled in **d**. Blue dotted lines show the observed present-day ice-sheet bed, ocean floor and ice surface[30], remapped on to the 15 km grid of the ice-sheet model.

Extended Data Figure 4: The drivers of re-advance and the impact of bed re-mapping. a and b, Results from four simulations (the reference simulation, and three additional experiments) designed to examine the cause of re-advance in the **a,** Weddell and **b,** Ross Sea sectors (Methods). The most inland GL location in the reference simulation around 10 kyr BP is in blue. The colour map shows the flow buttressing number[97] at 9.5 kyr BP for the 'No uplift, grounding of ice rises' experiment. The ice front position is in grey. Background images over the grounded ice sheet are from MOA (ref. 34). **c,** Basal topography and bathymetry in the Weddell (GL in red) according to a 1 km resolution dataset, constrained by geophysical observations (Bedmap 2; ref. 30). **d,** Conservative remapping of these data to 15 km resolution. Remapping significantly lowers the apparent maximum bed elevations beneath ice rises in the Weddell Sea Sector: 135 m at Korff Ice Rise (KIR), 112 m at HIR, 36 m at Bungenstock Ice Rise (BIR). The present-day GL is in red[30].

Extended Data Figure 5: True and apparent ages of radiocarbon. Eleven grey lines show the exponential ^{14}C decay curves connecting the $^{14}C/^{12}C$ ratios (scale on the left-hand-side axis) measured on AIO from our subglacial sediment samples to the apparent radiocarbon ages calculated from these measurements. The latter calculation assumes that the initial $^{14}C/^{12}C$ ratios in AIO was equal to the modern ratio in radiocarbon dating standards. As discussed in the text and methods sections, organic matter in Antarctic glacigenic sediments frequently contains an admixture of old ^{14}C-dead material[44,45]. The record of oxygen isotopes in water ice from the WAIS Divide ice core (green line with scale on the right-hand-side axis) provides climatic context for the period between now and 35 kyr BP (ref. 98). Three key climatic periods are labeled: WAIS LGM = Last Glacial Maximum for WAIS[99], ACR = Antarctic Cold Reversal, and Holocene.

Extended Data Figure 6: Model sensitivity to forcings. Time series of GL migration demonstrating model sensitivity in the Weddell (middle panels) and Ross (right panels) sea sectors to different **a,** sea-level reconstructions[70,79,80,81], **b,** scalings of the sea-level forcing to mimic self-gravitational effects, **c,** surface temperature forcings and **d,** accumulation forcings. The constant LGM accumulation uses the EPICA Dome C core[84] and a scaling of 2% per degree. Temperature and accumulation are expressed relative to the present-day. GL positions are relative to present day position (vertical dashed line) along transacts shown in Fig. 3. In all simulations the GL is in its most advanced position, up to 1000 km beyond its present-day position, before MWP1a (14.4 kyr BP, horizontal dotted line). During the Holocene the GL retreats up to 500 km upstream of its current location and usually re-advances towards its present-day position. Grey shading indicates spread of GL response and grey curves show the mean of each sensitivity experiment. In each case the violet curve shows the reference simulation. GL positions (based on marine and terrestrial geological evidence) from the RAISED reconstruction with associated uncertainty are shown in black[2].

Extended Data Figure 7: Model sensitivity to parameters. Time series of GL migration showing model sensitivity in the Weddell and Ross sea sectors to **a,** mantle viscosity μ, and the flexural rigidity of the lithosphere, D, **b** and **c,** enhancement factors E_{SSA} and E_{SIA}, **d,** sliding law exponent q, **e** till water decay rate T and till effective pressure fraction N, **f,** minimum till friction angle and the method used to derived friction angle (Methods), **g** PICO ocean model parameters for overturning strength C and heat exchange g and **h,** the dependence of calving rate on ice-shelf spreading rate K (Extended Data Table 2). In each panel the violet curve shows the reference simulation. GL positions (based on marine and terrestrial geological evidence) from the RAISED reconstruction with associated uncertainty are shown in black[2].

Extended Data Figure 8: Model sensitivity to spatial resolution. The results of three simulations using different grid resolutions: **a,** 15 km (reference simulation; identical to Fig. 3), **b,** 10 km and **c,** 7 km. Due to computational limitations the two higher resolution simulations only cover the last 35 kyr, so lack a higher resolution spin-up period, but display similar Holocene retreat and re-advance driven by isostatic rebound to the reference simulation. However, LGM extent and GL re-advance in the Weddell Sea are significantly smaller in the higher resolution simulations. A full exploration of the resolution dependence of the model requires using higher resolution during entire simulations for all ensemble members. This is currently limited by computing resources. Background shading shows basal topography and bathymetry[30].

Extended Data Table 1. Results of radiocarbon and $\delta^{13}C$ **analyses of subglacial sediments**. Carbon isotope results, including percent modern carbon, calculated age, analytical error and independently measured $\delta^{13}C$. Low percent modern carbon relative to dominant ancient (radiocarbon dead) carbon skews apparent ages older than the actual age of the marine connection discussed here. The light $\delta^{13}C$ results also point to a significant old carbon source.

UpB is the upstream portion of the WIS.

Extended Data Table 2. Key model parameters with modelled retreat and re-advance. Key model parameters that have been varied as part of a sensitivity study of our ice-sheet model (Methods). In each case the value used in the reference simulation is given as well as the range over which the parameters were varied during the sensitivity study. Also provided is a summary of the impact this parameter has on the model behavior in relation to the retreat of the GL past its present-day location and subsequent re-advance. See Methods for a detailed discussion of model sensitivities.

References

[96] Jezek K. C., Curlander J. C., Carsey F. Wales C. & Barry R. G. RAMP AMM-1 SAR Image Mosaic of Antarctica, Version 2. Boulder, Colorado USA. NSIDC: National Snow and Ice Data Center. doi: http://dx.doi.org/10.5067/8AF4ZRPULS4H (2013).

[97] Fürst, J. J. Durand, G. Gillet-Chaulet, F. et al. The safety band of Antarctic ice shelves. *Nature Climate Change* **6,** 479–482 (2016).

[98] WAIS Divide Project Members. Precise interpolar phasing of abrupt climate change during the last ice age. *Nature* **520,** 661–665 (2015).

[99] Clark, P. U. Dyke, A. S. Shakun, J. D. et al. The last glacial maximum. *Science* **325,** 710–714 (2009).

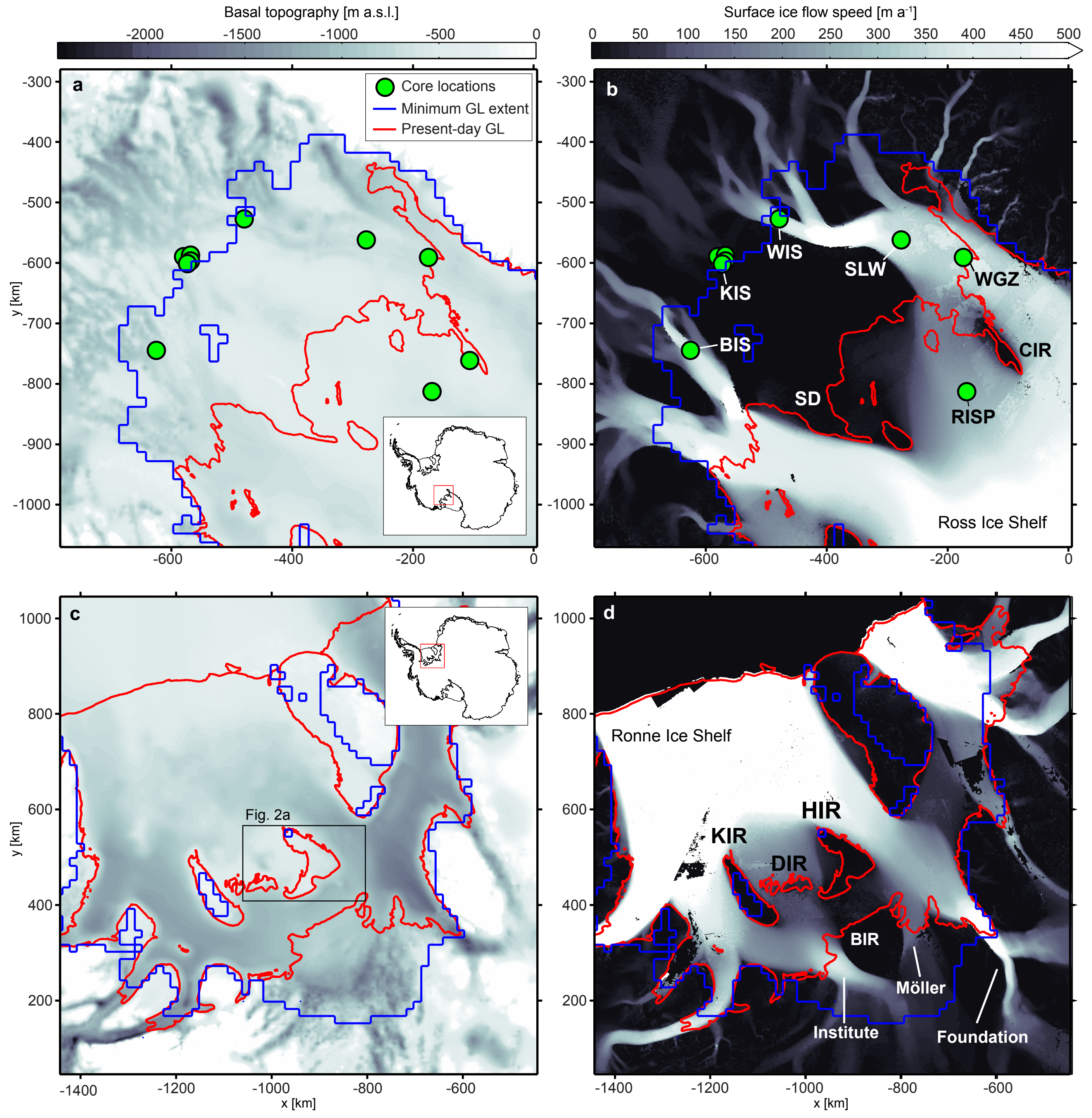
Basal topography [m a.s.l.]
Surface ice flow speed [m a^{-1}]
a
b
c
d
Core locations
Minimum GL extent
Present-day GL
WIS
SLW
KIS
WGZ
BIS
CIR
SD
RISP
Ross Ice Shelf
Ronne Ice Shelf
Fig. 2a
HIR
KIR
DIR
BIR
Möller
Institute
Foundation
y [km]
x [km]

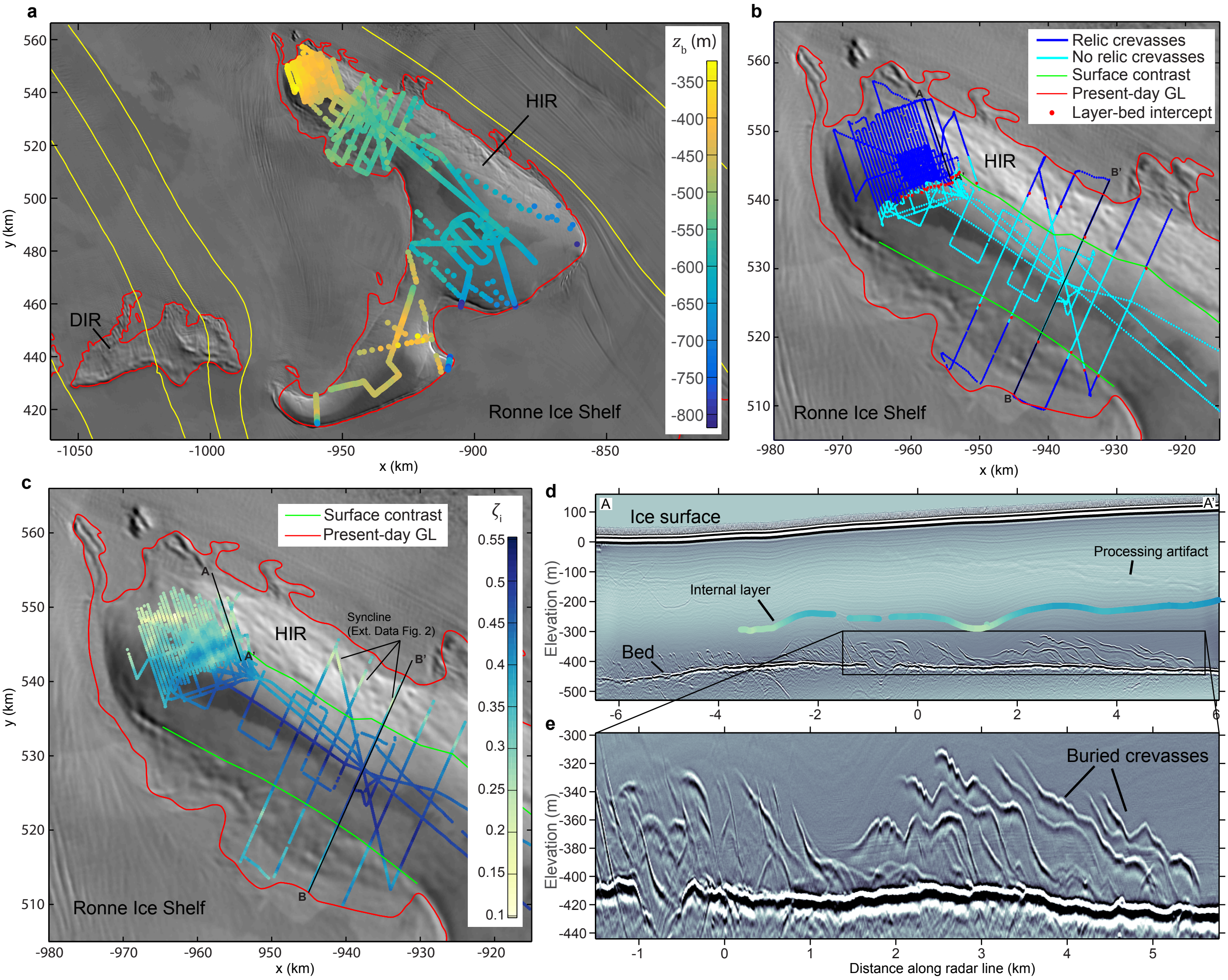

a
z_b (m)
-350
-400
-450
-500
-550
-600
-650
-700
-750
-800
HIR
DIR
Ronne Ice Shelf
y (km)
x (km)
b
Relic crevasses
No relic crevasses
Surface contrast
Present-day GL
Layer-bed intercept
HIR
Ronne Ice Shelf
c
Surface contrast
Present-day GL
ζ_i
HIR
Syncline
(Ext. Data Fig. 2)
Ronne Ice Shelf
d
Ice surface
Processing artifact
Internal layer
Bed
Elevation (m)
e
Buried crevasses
Elevation (m)
Distance along radar line (km)

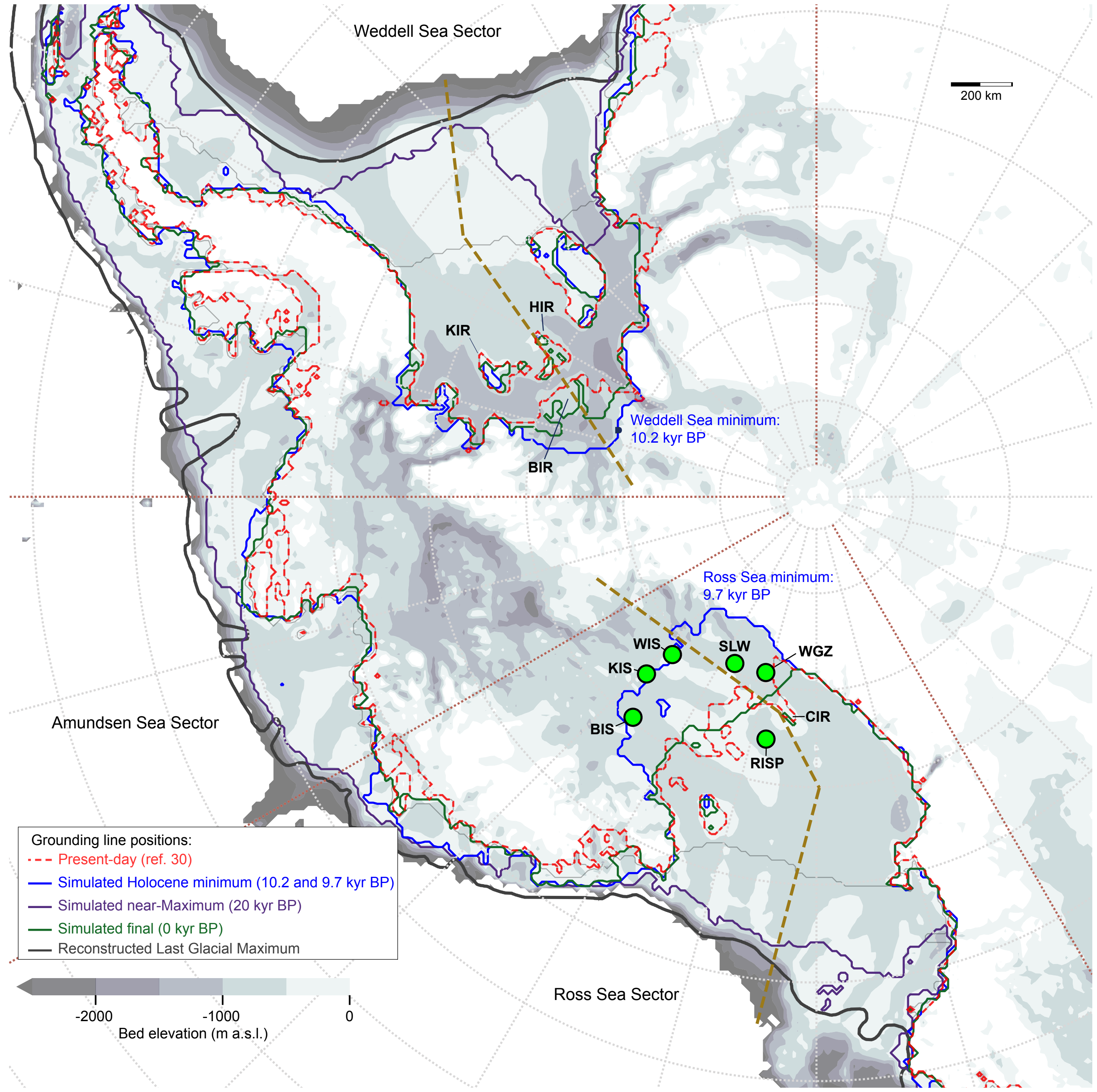

Weddell Sea Sector
200 km
HIR
KIR
Weddell Sea minimum:
10.2 kyr BP
BIR
Ross Sea minimum:
9.7 kyr BP
WIS
SLW
WGZ
KIS
CIR
BIS
RISP
Amundsen Sea Sector
Grounding line positions:
Present-day (ref. 30)
Simulated Holocene minimum (10.2 and 9.7 kyr BP)
Simulated near-Maximum (20 kyr BP)
Simulated final (0 kyr BP)
Reconstructed Last Glacial Maximum
-2000
-1000
0
Bed elevation (m a.s.l.)
Ross Sea Sector